UNIVERSITÀ DEGLI STUDI DI PADOVA

DIPARTIMENTO DI INGEGNERIA INDUSTRIALE

CORSO DI LAUREA MAGISTRALE IN INGEGNERIA DEI MATERIALI

Tesi di Laurea Magistrale in Ingegneria dei Materiali

TiO$_2$- CdS NANOSTRUCTURES FOR HYDROGEN PRODUCTION

Relatore: Prof. Giovanna Brusatin
Correlatore: Prof. Fayna Mammeri

Laureando: Mattia Pasut

ANNO ACCADEMICO 2012 – 2013

Introduction

The word's energy demand in the modern era is growing year after year and it will grow even faster in the near future. Both in the developed and in the developing countries the search for abundant energy sources, able to support the economic system, is becoming a primary issue.

Today, most of the energy demand is fulfilled by fossil fuels (petroleum derived, natural gas and coal), which are being depleted fast. Moreover, their combustion products are the main cause of several problems such as: pollution, greenhouse gases release in atmosphere, reduction of the ozone layer, which are putting in danger the natural environment and our health. Considering all these matters and the dangers of the nuclear power, showed after Chernobyl and recently highlighted in Fukushima, the need to find alterative sources has become an hard challenge.

Traditional renewable energy sources, such as: solar, wind, geothermal and hydroelectric, may not alone answer to the enormous energy demand. It is firstly, because of their actual cost which is not competitive compared to the cost of the energy produced with fossil fuels. Moreover their efficiency, at the present time, is not sufficient to make them economically and technically convenient without important state financial aids. And finally, they are fickle energy sources which are not assuring a constant supply of energy. The last problem proposed may be solved finding a safe way to stock the energy produced by them into an energy vector, which can be used where and when it is needed (the main example is the transportation field).

The hydrogen produced by electrolysis of the water using electricity, and the latter produced with renewable sources, may be an answer to the energy storage problem. Hydrogen is an efficient and clean fuel. Its main combustion product is water with a small amount of NO_x and pollution and no greenhouse gases. It may provide the connecting point between the renewable energy production and the transportation.

An even more interesting option is the direct production of hydrogen from renewable sources such as solar light. The pioneering studies have been carried out by Fujishima and Honda (1) in 1972, they first showed that a photo-electrochemical cell may be used for the hydrogen generation through the decomposition of water by using a TiO_2 photo-anode. Since the first studies the prospect to produce hydrogen directly from the sun light

using photo-electrochemical techniques has raised a lot of attention mainly because of the possibility to synthesize a fuel directly from an abundant and scattered energy source. Unfortunately, at the moment, the conversion efficiency achieved with the so far developed photo-anodes is not enough to give at this technique an economical interest. But a lot could be done engineering and projecting photo-anodes which show good photo-corrosion resistance and good stability in the working environment coupled with a good solar light conversion efficiency. Between the large varieties of semiconductors able to perform water splitting TiO_2 has gained a lot of interest due to its high stability and corrosion resistance. The main problem using TiO_2 as photo-anode is related above all to its low light harvesting ability. This problem is mainly due to its wide band gap (3.2 eV) which makes it able to use only the UV region of the solar spectrum for water splitting. Therefore only a fraction of the energy provided by the solar light is stored in the form of gaseous hydrogen. Several pathways have been developed in order to enhance the light harvesting of the TiO_2 and improve its hydrogen production efficiency. This work is focused over one of them: the coupling of TiO_2 with a narrow band gap semiconductor, in our case CdS. This method allows to extend the light harvesting to the near visible region increasing the fraction of the solar spectrum used for water splitting. We tried to develop an high efficiency photo-anode coupling TiO_2 nanofibers and CdS quantum dots in order to create a nanocomposite material.

My thesis work is organized in two main parts: the first one is focused over the theoretical aspects of hydrogen production by photo-electrochemical water splitting and the samples production techniques, whereas the second part presents the results of the characterization and photo-electrochemical tests over the produced samples.

The first part of the work is divided as following:
- The first and second chapters present an brief introduction concerning the methods employed for hydrogen production and an historical outline on photo-electrochemical water splitting.
- In the third chapter I am presenting a theoretical dissertation on the mechanism of photo-electrochemical water decomposition.
- Chapters four and five discuss the influence of the solar spectra on the efficiency of the photo-electrochemical cell and the properties of the photo-electrodes.

- The sixth chapter presents a brief introduction on the TiO_2 and the methods used to enhance the light harvesting and the its efficiency as a photo-anode.

The second part, presenting the whole experimental part (techniques employed and the results obtained), is divided as follow:

- Chapters eight and nine presents the techniques used for the samples production, focusing on the polyol process (for the synthesis of CdS quantum dots, QDs) and the hydrothermal process (for the preparation of TiO_2 nanofibers).

- In chapter ten, I am presenting the results of the characterization dividing them in three sections:

- in the first one are showed the results obtained for the characterization of the CdS QDs
- in the second one the results obtained for the TiO_2 nanofibers
- and finally in the third one are presented the results obtained for the nanocomposites made coupling the TiO_2 nanofibers with the CdS quantum dots.

- In chapter eleven the photo-electrochemical tests carried out are briefly described and the results are presented. We focused our attention over two techniques employed for cheking the response of the produced samples under illumination: cyclic voltammetry and chronoamperometry.

1. Hydrogen

1.1.   Introduction

Hydrogen is considered as the fuel of the future, and many efforts have been done in order to develop technologies based on the application of hydrogen instead of fossil fuels. Hydrogen as an energy carrier, coupled with green production technologies may lead to a sustainable energy system. Hydrogen is versatile fuel, it can be converted in other forms of energy in different ways: converted to heat through flame or catalytic combustion, converted directly to steam and converted directly to electricity through electrochemical processes (2). In other words hydrogen, as a fuel, can be converted through more than one process to different forms of energy ready to be used by the final consumer.

Moreover, if we focus on the combustion of hydrogen, it does not produce any CO_2, CO, SO_x, hydrocarbons and particulates, except some NO_x produced via flame combustion. The main product of the combustion is water, which neither results in pollution or greenhouse gasses and it leads to a substantial reduction of the emissions. Therefore, it seems that the hydrogen is a zero emissions fuel, it is true if it is considered only the final utilization step (in this case the combustion). On the other hand if we consider all the system of hydrogen production and especially the extraction methods, we may arrive to a different result. In others words; hydrogen is not present in a gaseous form in nature. However it is available in several compounds such as plants, methane, methanol, higher hydrocarbons and water. Therefore, it is necessary to extract it from these resources. So far, the hydrogen is produced above all using fossils resources, as is shown in Figure 1-1; in particular by steam reforming from of natural gas 48% (3).

The production from other fossil fuels, coal and oil is essentially obtained by the process of partial oxidation, exposed in sections 2.2.2, 2.2.3 .
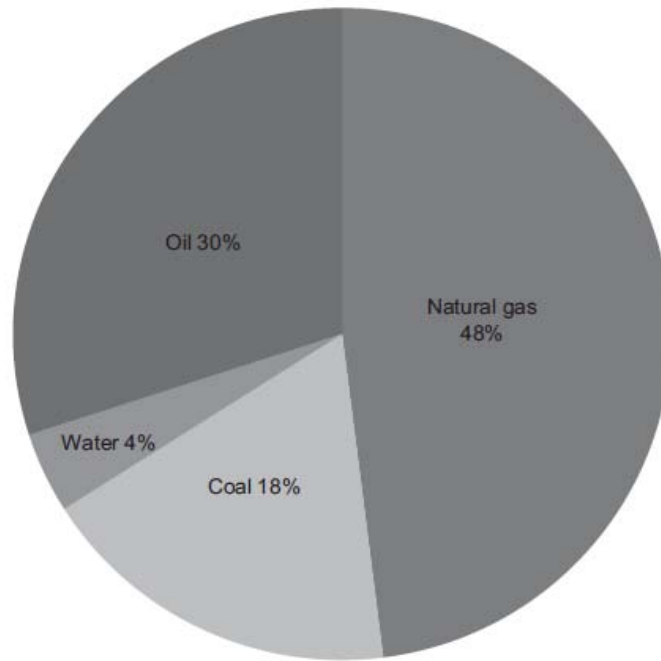
Figure 1-1 Distribution of the hydrogen production ways (3).

These methods of production are clearly not solving the problems related to the CO_2 emissions and the fossil fuels dependence. Chapters 2.2.1, 2.2.2 and 2.2.3 describe briefly the above mentioned H_2 production processes. Only 4% of the hydrogen is produced by water electrolysis (3). This method does not contribute directly to the CO_2 emissions, the water molecule is split applying a potential between two electrodes dived into distilled water and so producing gaseous oxygen at the anode and hydrogen at the cathode. The problem in this case is how the electricity is produced. Considering that the electricity generation accounted for 39% of the global carbon emissions in 2000 (4), it is easy to understand that this can not be an environmental friendly solution. A way that is possible to walk through is the partial substitution of the traditional electricity production methods with removable sources. The cost of the energy produced with removable technologies at the moment is bigger than the traditional sources and their contribution to the total electricity production is low, moreover, the intermediate passage of the electricity production leads to energy loss.

On the other hand, the production of hydrogen directly from solar energy may be a promising solution. Solar energy is potentially the most abundant renewable energy source, unfortunately it is an irregular and difficult to store source. The use of photo-electricity could be considered as a good option for the hydrogen generation. In this case the hydrogen offers a way to convert an non-storable source (sun light) directly in a storable fuel (hydrogen), ready to be used in a large number of applications.

The energy conversion efficiency for water photolysis is mainly determined by the characteristics and properties of the material used as photo-electrodes. So the performance of the photo-electrochemical cells (PEC), and consequently the commercial applications, depends on the progress in material science and engineering applied to the materials used as photo-electrodes.

1.2.   Currently most common hydrogen production process

In this section are briefly presented the main methods currently used for industrial large scale hydrogen production.

1.2.1. Natural gas reforming

Most hydrogen produced today is made by natural gas reforming (3). Natural gas contains methane (CH_4) that can be used to produce hydrogen with thermal process. In this process high temperature steam (700 °C- 1000 °C) reacts with methane under 3-25 bar pressure in presence of catalyst producing: hydrogen and carbon monoxide (Equation 1). This reaction is endothermic, so it is necessary to supply heat in order to implement the reaction.

Then the carbon monoxide and steam react in presence of a catalyst producing carbon dioxide and more hydrogen (Equation 2). Then, hydrogen is separated and purified. (5)

$$CH_4 + H_2O(+heat) \rightarrow CO + 3H_2 \qquad (1)$$

$$CO + H_2O \rightarrow CO_2 + H_2 \qquad (2)$$
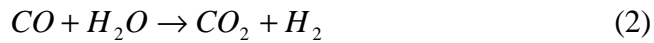
1.2.2. Oils reforming

Ethanol, bio-oils or other liquid fuels can be processed in order to produce hydrogen. The method is similar to the natural gas steam reforming. The liquid fuel reacts with steam at high temperatures in presence of a catalyst to produce hydrogen and carbon monoxide. Then, additional hydrogen is produced reacting carbon monoxide with high temperature steam.

1.2.3. Coal gasification

Hydrogen can be produced from coal by coal gasification. First, coal reacts with oxygen and steam at high temperatures and pressures to form a synthesis gas, mixture mainly constituted of hydrogen and carbon monoxide (Equation 3). Then, the impurities are removed and the carbon monoxide is reacted in order to produce additional hydrogen (Equation 2).

$$CH + O_2 + H_2O \rightarrow CO + CO_2 + H_2 + other\ species \qquad (3)$$
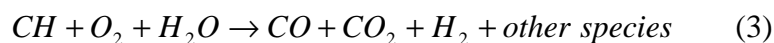
1.2.4. Water electrolysis

During electrolysis the electricity is used to split the water molecules in gaseous hydrogen and oxygen. The reaction takes place in a unit cell composed of one anode and one cathode dived in water and connected through an external circuit. A difference of potential is applied between the electrodes and water reacts at the anode forming gaseous oxygen, electrons and hydrogen ions (Equation 4). Then, the electrons flows through the

external circuit and the hydrogen ions migrate through the electrolyte to the cathode. At the cathode, hydrogen ions can combine with the electrons arriving from the external circuit leading to the formation of gaseous hydrogen (Equation 5).

$$2H_2O \rightarrow O_2 + 4H^+ + 4e^- \quad \text{Anode reaction} \quad (4)$$

$$4H^+ + 4e^- \rightarrow 2H_2 \quad \text{Cathode reaction} \quad (5)$$
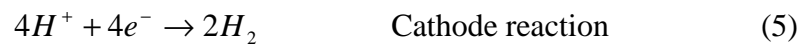
2. Photo-electrochemical hydrogen production: Historical outline and state of the art

In this chapter, I present a brief summary of the main stages that lead to the hydrogen production by photo-electrochemical water splitting.

1839: Becquerel effect

The discovery of the photo-electrochemical effect was made by Becquerel in 1839 (6). Studying the AgCl/electrolyte/metal system he observed a current flow between AgCl and the metal electrodes when AgCl was exposed to light. This discovery putted the bases for the photo-electrochemical technology.

1954: Theory of photo-electrochemistry

The theory of semiconductors, made by Brattain and Garret (7), has led to theoretical explanation of the Becquerel effect. It explains the charge transport in terms of band model theory. This theory was then developed by Gerischer (8), Memming (9) and Morrison (10).

1972: Hydrogen generation using photo-electrochemical devices

Fujishima and Honda (1) first showed that a photo-electrochemical (PEC) cell may be used for the hydrogen generation through the decomposition of water by using a TiO_2 photo-anode. This discovery indicated that it is possible to produce gaseous hydrogen using solar light through PEC technology. They also evidenced that oxide materials exhibiting a high corrosion resistance may be used as photo-electrodes.

1975-1976: Oxide Materials as photo-electrodes and firsts attempts to modify TiO$_2$ properties

The work of Fujishima and Honda (1) is a real breakthrough in the field of semiconducting materials exhibiting suitable properties for the solar water splitting. Researchers also thought the possibility to modify the semiconducting properties of the TiO$_2$ in order to improve them and achieve the characteristics of the ideal photo-anode described by the theory.

Then, the research focused on the TiO$_2$, identifying it as the best candidate for the production of photo anodes. Several studies demonstrate that its light absorption can be increased by modifying its semiconducting properties. Several pathways have been followed, among them: noble metal loading (11), ion doping (12), dye sensitization (13), carbon doping (14), composite semiconductors (15). In all the cases the first goal was to enhance the light harvesting of the TiO$_2$ photo-anode in order to reach a higher efficiency in the solar conversion.

3. Mechanism of photo-electrochemical water splitting

The aim of this section is to explain the principles and the mechanisms that lead to the water decomposition by photo-electrochemical route.

3.1. Principles

The main principle of the photo-electrochemical water decomposition is based on the conversion of solar light energy in electricity in a cell equipped with two electrodes, immersed in an electrolyte: where one of them is a semiconductor able to absorb the solar light, if exposed to it. The electricity produced is then used for the water electrolysis and the consequent production of H_2.

3.2. Reaction mechanism

The water photo-electrolysis involves several processes within the photo-electrodes and the photo-electrodes interface:

- Light induced intrinsic ionization of the semiconducting material (anode), and the consequent formation of electronic charge carriers (excitons or electron-holes pairs)
- Oxidation of water by the holes at the anode
- Transport of H^+ ions from the anode to the cathode through the electrolyte and transport of the electrons from the anode to cathode through the external circuit
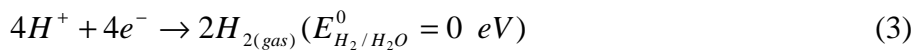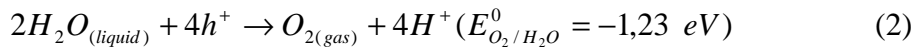- Reduction of H^+ ions at the cathode

The electronic structure of the semiconductor is characterised by the presence of a valence band (VB) and a conduction band (CB). The smallest energy difference between the top level of the VB and the bottom level of the CB is called band gap (E_g).

At the ground state electrons are in the VB, whereas when the semiconductor is excited by a photon with energy equal or higher than the band gap energy level an electrons is promoted from the VB to the CB creating a photo-generated electron/hole pair, (Equation 1).

$$4h\upsilon \rightarrow 4e^- + 4h^+ \tag{1}$$

Where h is the Planck's constant, υ the frequency, e^- the electron and h^+ the hole.

Usually the photo-generated electrons can recombine within short time, releasing energy in form of heat. The holes produced and not recombined split the water molecules in gaseous oxygen and hydrogen ions, as shown in equation 2.

$$2H_2O_{(liquid)} + 4h^+ \rightarrow O_{2(gas)} + 4H^+ (E^0_{O_2/H_2O} = -1,23\ eV) \tag{2}$$

$$4H^+ + 4e^- \rightarrow 2H_{2(gas)} (E^0_{H_2/H_2O} = 0\ eV) \tag{3}$$

Reaction 2 takes place at the anode/electrolyte interface. O_2 is produced at the anode and the H^+ ions migrate to the cathode through the electrolyte. At the same time, the electrons are transferred through the external circuit to the cathode and here they reduce the H^+ into gaseous hydrogen, as shown in equation 3. The overall reaction may be expressed as:

$$4h\upsilon + 2H_2O_{(liquid)} \rightarrow O_{2(gas)} + 2H_{2(gas)} \tag{4}$$
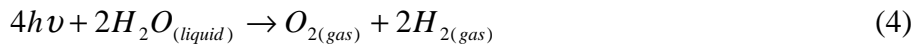
Reaction 4 takes place only when the following conditions are satisfied:

- The conduction band level should be more negative than hydrogen production level ($E_{H2/H2O} = 0$ eV) for hydrogen production
- The valence band level should be more positive than the water oxidation level ($E_{O2/H2O} = -1.23$ eV) for oxygen production

The theoretical photon energy required to start the reaction 4 is E_t=1.23 eV, the same value than the ideal semiconductor band gap. In other words, the electrochemical decomposition of the water takes place when the electromotive force of the cell is equal or larger than E_t=1.23 eV (16).

Therefore, theoretically the lowest limit of the band gap is determined by the energy required to split the water molecule, as discussed in the previous section it is equal to E_t=1.23 eV. In practice, the energy required is bigger, this is due to the energy losses caused by:

- Polarization within the photo-electrochemical cell
- Recombination of the electron-hole pairs
- Resistance of the electrodes
- Resistance of the electrical connections

The estimated value of all the above mentioned losses is equal to $E_l \approx$ 0.8 eV (16). Therefore, the energy limit required to allow the water splitting is the sum of: the lowest energy required (E_t=1.23 eV) and the energy losses ($E_l \approx$ 0.8 eV). Thus we obtain $E_i \approx$ 2 eV. Therefore, the practical minimum energy required for starting reaction 4 is equal to $E_i \approx$ 2 eV and only photons with energy higher or equal to E_i can be used for water splitting. However the effective use of this photons depends on the presence of a semiconductor with band gap equal to $E_g = E_i$. Hence, E_i has to be considered as minimum band gap width for a semiconductor able to split water molecules. Unfortunately, the common semiconductors exhibiting this optimal band gap width are easily corroded. Among them: Fe_2O_3 (E_g= 2.3 eV) (17), GaP (E_g =2.23 eV) (18), GaAs (E_g= 1.4 eV) (18), CdS (E_g= 2.4 eV) (19). Figure 3-3-1 shows band gaps positions of several semiconductors in contact with aqueous electrolyte at pH=1. The lower edge of the conduction band (red) and the upper edge of the valance band (green) are presented with the band gap width value in electron volts eV. The energy scale is indicated in eV using either the normal hydrogen electrode (NHE) or the vacuum level as reference.
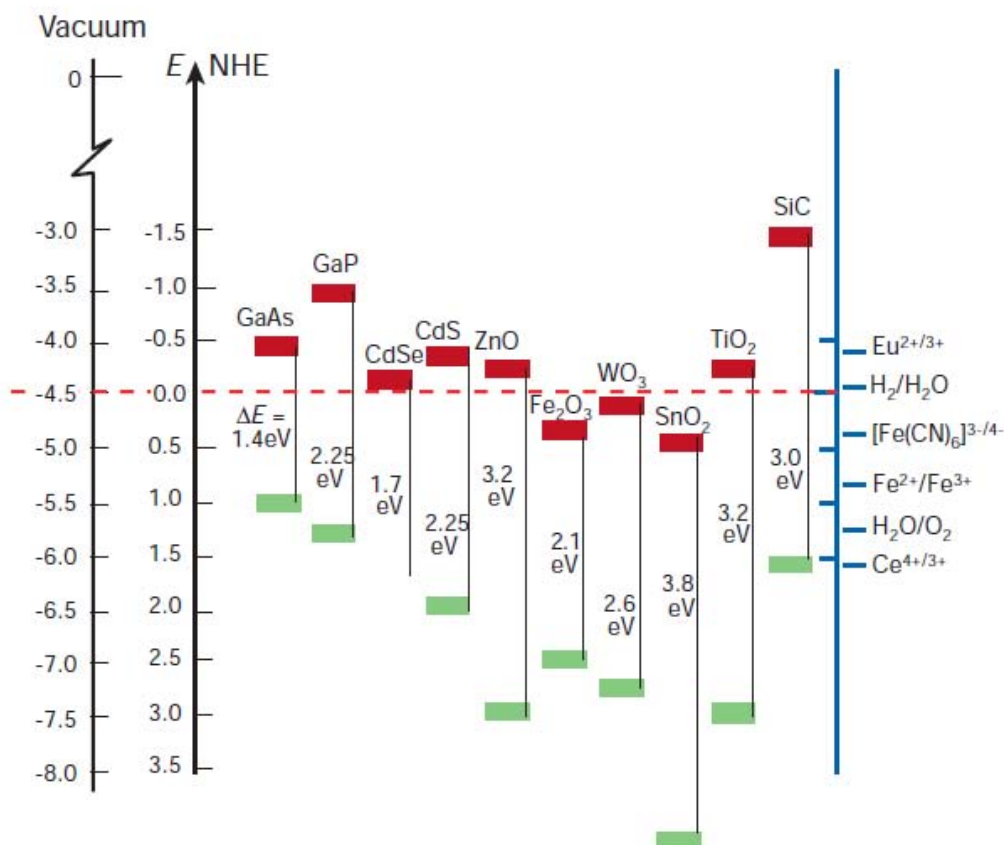
Figure 3-3-1 Positions of several semiconductors in contact with an aqueous electrolyte at pH=1(21).

TiO_2 is the most studied photo-anode, but its band gap is equal to 3.2 eV: therefore, the part of the energy spectrum available for the water splitting process becomes smaller. Despite its high band gap, the TiO_2 has got special attention thanks above all to is high corrosion resistance in the working environment employed in water splitting.
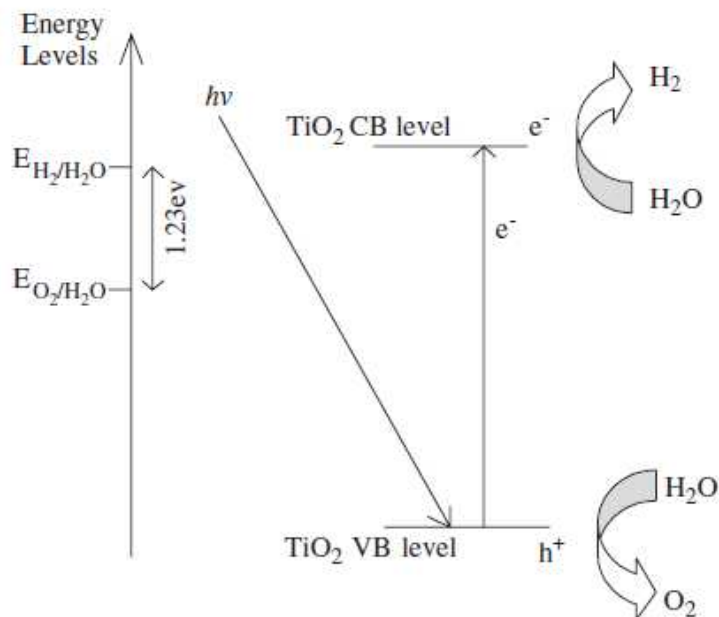
Figure 3-2 Schematic mechanism of photo-electrochemical water decomposition using TiO_2 (29).
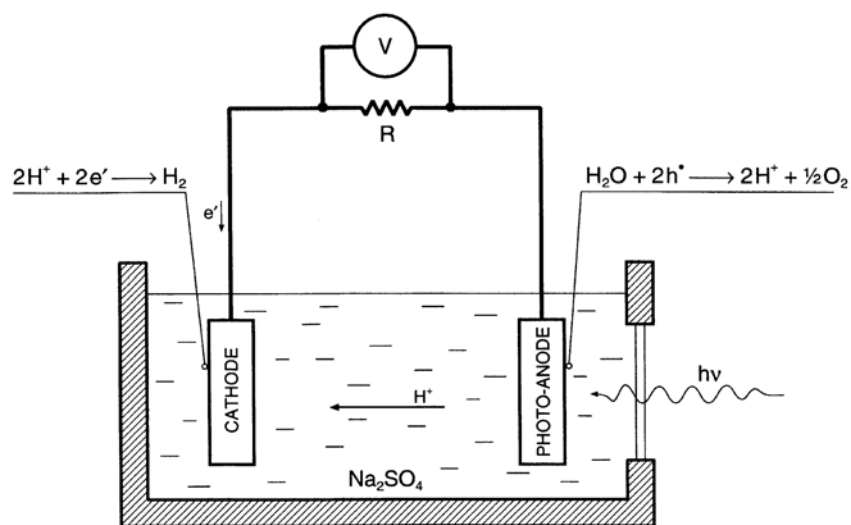
Figure 3-3 Representation of photo-electrochemical cell (16).

Figure 3-3 depicts a representation of a typical photo-electrochemical cell, involving a photo-anode (metal oxide) and a cathode (Pt) immersed in an aqueous solution (electrolyte). The charge transport includes the electrons migration through the external circuit and the hydrogen ions migration through the electrolyte, resulting in the production of hydrogen and oxygen at the cathode and anode respectively.

3.3.   *Photo-catalytic water splitting*

Considering the mechanism of reaction, photo-catalytic water splitting follows similar principles than the photo-electrochemical water splitting. The main difference is the location where the reactions of reduction of the hydrogen ions and of oxidation of water.

In the photo-electrochemical process these reactions occur in two different places, respectively the photo-anode and the cathode, physically distinct. In the photo-catalysis process both oxidation and reduction happen at the surface of the catalyst. Hence, in a photo-electrochemical process hydrogen and oxygen evolve separately while in photo-catalysis, a mixture of hydrogen and oxygen is produced, which have to be further isolated. (20)

4. Influence of the photo-electrode properties on the solar energy conversion

This chapter is focused on the influence of the band structure of the photo-electrode on the solar energy conversion efficiency. It is possible to consider the solar spectrum in terms of number of photons vs photon energy as shown in Figure 4-1.
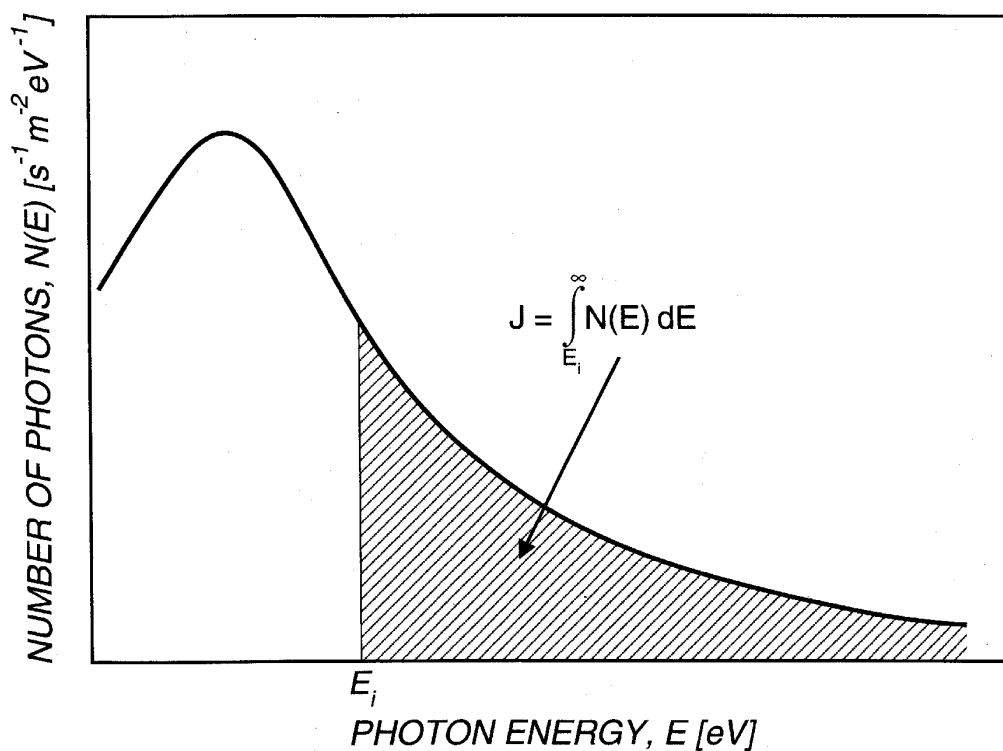

Figure 4-1 Illustration of the light spectrum showing the flux of photons available for conversion (16).

The area highlighted below the curve corresponds to the flux of photons J of energy equal or higher to E_i:

$$J = \int_{Ei}^{\infty} N(E)dE \qquad [s^{-1}m^{-1}]$$

Where N(E) is the distribution of photons as a function of their energy, E is the energy of the photons, and E_i is the threshold energy.

The part of the spectrum below this energy threshold is not available for the conversion The value of the band gap of the material used has an important role on the energy conversion of photons. Only the photons of energy equal or larger than that of the band gap may be absorbed and participate to the electron-hole pair's production. As discussed in the previous chapter, only photons of energy higher or equal to E_i may be used in water splitting. Therefore, a semiconductor with a band gap E_g value near E_i shows a higher value of J than a semiconductor with a wider band gap. In other words, a semiconductor with narrow band gap can absorb a higher number of photons, suggesting the production of an higher number of electron-hole pairs produced and so an higher efficiency of the photo-anode.

The solar energy can be also considered in terms of energy E over wavelength λ, as shown in Figure 4-2. The conversion of the solar energy is determined by the part of the spectrum whose photons of energy equal or higher than the minimum value request for the water splitting reaction: E_i. The area under the spectrum is defining the incidence of solar irradiance I_r, $λ_i$ is the value of the wavelength related to the minimum energy E_i necessary to start the water splitting.

$$I_r = \int_0^{\lambda i} E(\lambda)d\lambda \qquad [\text{Wm}^{-2}]$$

$$I_r = \int_0^{\lambda_i} E(\lambda)\, d\lambda$$
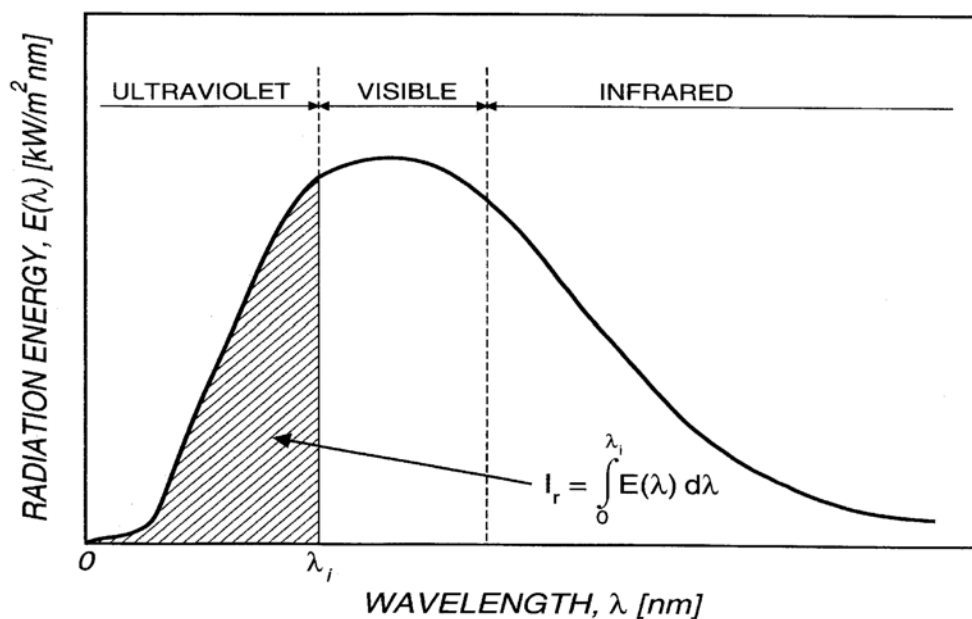
Figure 4-2 Representation of the light spectrum showing the incidence of solar irradiance I$_r$ available for conversion (16).

One can notice in Figure 4-2 that shifting the absorbance of the semiconductor to the near visible region makes possible to use the part of the solar spectrum which shows higher values of radiation energy. It is thus of interest, to develop a semiconductor able to absorb in the visible range of wavelengths (from 400 nm to 700 nm corresponding to approximately, band gap values from 3 eV to 1.7 eV) in order to use parts of the spectrum where can be found more photons with enough energy to start the water splitting reaction.

The challenge is to process a corrosion resistant material with a band gap narrow enough to be able to absorb photons in the visible and near visible region. To do that there are several pathways which can be followed and they will be discussed in chapter 6.

5. Properties of the photo-electrodes

Materials used for photo-anodes have to satisfy several properties. Although few materials have been identified, none of them satisfy all the requirements. In this section, I present a summary of the most important properties required for high performances photo-anodes.

5.1.   Band gap

The band gap, E_g, is the smallest energy difference between the top of the valence band VB and the bottom of the conduction band (CB). The width of the band gap is a key parameter, influencing considerably the absorption of the photons and thus the generation of electrons-holes pairs. It has been discussed in the previous section that the optimal band gap for high performance photo-electrodes is ≈ 2 eV (22). A material satisfying this requirement and resistant enough to corrosion in aqueous environment it is not currently commercially available. That's why most of the studies developed to process such a material consist in the tailoring of the TiO_2 band gap. Indeed TiO_2 exhibits a strong chemical stability and an high corrosion resistance. Several methods to achieve this purpose have been developed and hey will be briefly discussed in the following sections. During my internship I focused my study on the coupling of TiO_2 structures with a narrower band gap semiconductor, in our case CdS (see the experimental section for more details).

5.2. Flat-band potential

The flat-band potential, U_{fb}, is the potential that has to be imposed over the electrode/electrolyte interface in order to make the bands flat (16). In other words, considering the idealized interface between a semiconductor and an electrolyte solution, in order for the to phases to be in equilibrium, their electrochemical potential must be the same. The electrochemical potential of the solution is determined by the redox potential of the electrolyte (in our case H^+/H_2 couple), and the redox potential of the semiconductor is determined by the Fermi level. If they do not lie at the same energy, in order to equilibrate the two phases is required a movement of charges between the semiconductor and the solution. The excess of charges is located in the semiconductor and it extends into the electrode for a significant distance (space charge region) and it has associated an electrical field. For n-type semiconductor electrode at open circuit the Fermi level is more negative than the redox potential of the electrolyte, hence the electrons flow from the electrode to the solution. Therefore, there is a positive charge associated with the space charge region and this is reflected in a upward bending of the band edges. Since the majority charge carriers has been removed from this region it is also referred as depletion layer. The magnitude and the direction of the band bending varies with the applied potential. At a certain applied potential the Fermi level lies at the same energy as the solution redox potential. There is no net transfer of charge and hence no band bending. This potential is defined flat-band potential U_{fb} (42). Considering the process of water splitting by photo-electrolysis it may take place if the flat-band potential is higher than the redox potential of the H^+/H_2 couple (16), which depends on the pH. Photo-anodes made of materials with flat band potential more negative respect the redox potential of the H^+/H_2 couple can split water molecules without the imposition of an external potential. Apart from the type of semiconductor the flat band potential depends on the nature and the composition of the electrolyte. For example in aqueous solutions the flat band potentials of most oxide semiconductors are shifted by 0,059 V when the pH is changed by one unit. This is a consequence of the fact that protons are potential-determining ions for these solids (21).
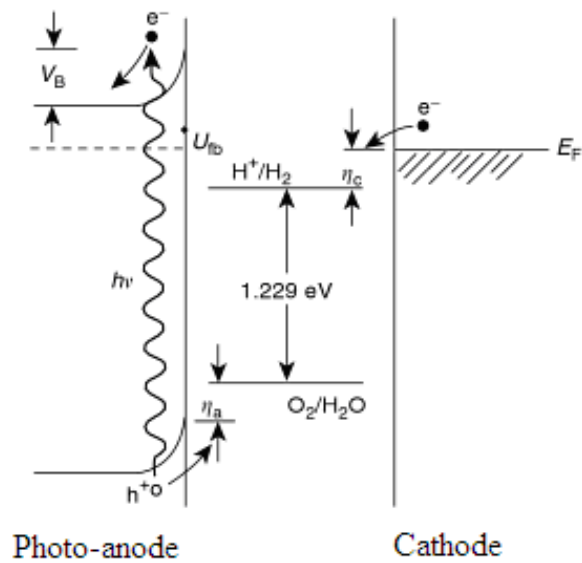
Figure 5-1 Level of a semiconductor n-type photo-anode where the flat band potential lies above H⁺/H₂ redox potential (16).

5.3. Schottky barrier

The potential drop within the interface between the semiconductor and the metal is named Schottky barrier. It plays an important role preventing the recombination of the charge carriers formed as a result of the illumination and so enhancing the efficiency of the photo-electrochemical device. High values of the Schottky barrier hinder potential recombination of the electron-hole pairs, the value of the barrier depends on the characteristics of both, metal and semiconductor.

5.4. Electrode electrical resistance

The electrical resistance of the semiconductor photo-anode is several orders of magnitude larger compared with that of the metallic cathode. Equation 1 describes the electrical conductivity in a semiconductor, which is determined by the concentration of the charge carriers and their mobility.

$$\sigma = en\mu_n + ep\mu_p \tag{1}$$

Where n is the concentration of electrons, p is the concentration of holes, μ_n the mobility of the electrons and μ_p the mobility of the holes. At high concentrations of the charge carriers mutual interactions causes a diminution of the charge carriers mobility. Therefore, the maximal σ results is dealing with the effect of increasing the concentration and decreasing the mobility.(16)

5.5. Helmholtz potential barrier

A semiconductor/electrolyte junction is formed when a semiconductor is immersed in an electrolyte. The chemical potential of the semiconductor is determined by the Fermi level, whereas the chemical potential of the electrolyte is given by the H^+/H_2 redox potential. If the initial Fermi level of the semiconductor is more negative respect to the initial electrolyte redox potential, the electrons will flow from the semiconductor to the electrolyte. The charge transfer induces a depletion region and a potential barrier (Figure 5-2). This surface charge is compensated in the electrolyte within a located layer ($\approx$ 1 nm thick) known as Helmholtz layer, constituted by oriented water molecules and electrolyte ions adsorbed on the electrode surface. The potential drop is determined by the nature of the aqueous environment of the electrolyte and the properties of the photo-anode surface. The performances of the PEC cell depends on the potential drop trough the Helmholtz barrier. For example for a n-type semiconductor, if the electron-holes pairs production

happens in the depletion region, the electric field in this region will cause a charge separation. The band edges curve upwards and the holes moves towards the interface while the electrons moves to the bulk of the semiconductor (23).
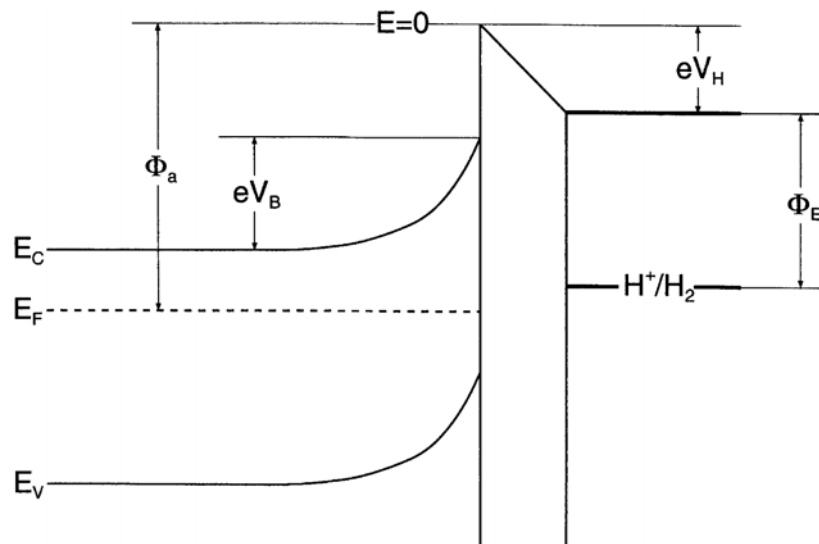

Figure 5-2 Energy diagram for a solid liquid interface consisting in a n-type photo-anode and a electrolyte (16).

5.6. Corrosion resistance

One has mention that photo electrodes (photo-anode in our case) have to exhibit good corrosion resistance during all the reactions taking place at the solid-liquid interfaces. The degradation of the photo-anode would lead to a change of its chemical composition and the its related properties, damaging its photo-conversion ability. Therefore, it is important for the photo-electrodes to avoid:

- Photo-corrosion
- Electrochemical corrosion
- Dissolution

Unfortunately, a large group of semiconductors, which exhibit good and suitable semiconducting properties for solar water splitting are also subjected to the previous reactions, leading to a drastic deterioration of their properties. To the best of our knowledge, TiO_2 is the semiconducting material which presents the best stability in aqueous environment and exhibits a good resistance to the photo-corrosion.

6. Titanium dioxide, TiO2

6.1. General information

Titanium dioxide (TiO_2) belongs to the family of transition metal oxides and owns three polymorphs in nature: anatase, brookite and rutile. The first large scale application of TiO_2, in the beginning of the 20th century, was to replace toxic lead oxides used as white pigment for paints. Now TiO_2 is used as white pigment in paints, plastics, papers, which represent the major end-use sectors. Other minor end-use sectors of TiO_2 as pigment such as textiles, food (food colorant (E-171), pharmaceuticals (tablet coatings, toothpaste, UV absorber in solar creams) have been developed in the following years.

Besides the pigment ability, other properties of TiO_2 have received a great deal of attention: chemical stability, non-toxicity and compatibility with the human body, low cost, high reflective index, photo-catalysis properties. All these characteristics have extended the application fields of the TiO_2. It is successfully used as gas sensor, due to the dependence of the electrical conductivity on the ambient gas composition. Due to its compatibility with the human body it is used as a biomaterial, above all as bone substituent. It is also used in catalytic reactions, reactions carried out with TiO_2 catalysis including selecting reduction of NO_x to N_2, decomposition of dioxins, CO oxidation by O_2, SO_2 reduction by CO.

Nanostructured TiO_2 is studied for applications in the field of photocatalysis, photolysis of water, light assisted degradation of pollutant and light induced superhydrophilicity (24).

6.2.   TiO₂ in photo-electrochemical applications

The TiO$_2$ is the most widely used material for photo-anode due mainly to its strong catalytic activity and chemical stability. The efficiency of the conversion from solar energy to hydrogen is low and that is due to the following reasons:

- Recombination of the electron/hole pairs releasing energy in the form of heat
- Fast backward reaction: reaction of recombination of hydrogen and oxygen into water
- The value of TiO$_2$ band gap 3.2 eV allowing to use only the UV light for hydrogen production. The inability to use the visible spectrum limits strongly the efficiency of the process.

The structure morphology of the TiO$_2$ plays an important role in the efficiency of the photo-catalysis for H$_2$ production. One dimensional structures (nanowires, nanorods, nanofibers) compared to the spherical particles could provide a high surface area and high interfacial charge transfer rate. The carriers are free to move through the length of the nanostructures, which is expected to reduce the e^-/h^+ recombination probability. (25) Therefore, introducing a dimension level nanofibers can achieve enhanced charge separation over colloidal systems, and shows better photo-current response. The high aspect ratio improves the charge transfer at the semiconductor/electrolyte interface, limiting the recombination process. Moreover, comparing nanofibers layers with flat surfaces, it is easy to understand that the nanofiber structure possess a higher surface/volume ratio, leading to a larger surface available for the light harvesting. Therefore, it is logical to expect that the increased aspect ratio of the nanofiber enhance the photocurrent density. Another advantage of nanofiber's structure, and in general of porous structure, is related to the possibility of easily soak them with nanoparticles of a narrow band semiconductor.

6.3. Enhancement of TiO$_2$ solar conversion efficiency

Several paths have been followed in order to solve the mentioned problems noticed in solar light conversion of TiO$_2$ and increase the efficiency of the hydrogen production from solar light. In this section we will be briefly present some of the main pathways which have been already developed.

6.3.1. Noble metal loading

Coating TiO$_2$ nanostructures by noble metals particles, such as Pt, Au, Pd, have been reported to be useful for the enhancement charge carriers separation in TiO$_2$ (27). These noble metals exhibit lower Fermi levels than that of the TiO$_2$, promoting the transfer of photo-excited electrons from the conduction band of the metal particle deposed over the surface of the TiO$_2$, while the photo-generated holes remain on the TiO$_2$. Therefore the probability of electron-hole pairs recombination is greatly reduced, resulting in an efficient charge separation. It is necessary to identify the optimal loading; too much metal particles present at the surface of TiO$_2$ may reduce the photon absorption by TiO$_2$ and consequently lower its efficiency. Another aspect that should be considered is the cost of the noble metals, very expensive.(29)

6.3.2. Ion doping

Ion doping is a method used for enhance the efficiency in light conversion of TiO$_2$. Two main schemes can be considered depending on the choice of the ion: metal ion (cation) doping or anion doping.

Metal ion doping method consists in incorporate transitional metal ion or rare earth metal ion into the TiO$_2$ lattice (28). As the ions are incorporate impurity, energy levels in the band gap of the TiO$_2$ are formed. Electron transfer between the ions and the TiO$_2$ can alter the electron-hole recombination, in other words the created energy levels can act as electron (or hole) traps. The reactions could occur only if the trapped electron and holes are transferred to the surface. Therefore the metal ions should be introduced near TiO$_2$

surface for a better charge transferring. In case of deeper doping metal ions may behave as recombination centres, so exist an optimal concentration of dope above which the efficiency observed decrease. Research in metal ion doping has been carried out particularly for water/air cleaning applications, but unfortunately these results can not be directly applied to the hydrogen production.(29)

Anion doping is an alternative method to enhance the photo-activity of TiO_2 incorporating in its crystalline lattice elements like: C, N, F. Anionic doping was found to be most effective than the metal ion doping because its p states can be mixed to the O2p states and thus contribute to the band gap narrowing (30).

6.3.3. Metal ion implantation

Metal ion implantation is an effective method to modify electronics structures of semiconductor materials in order to improve visible light harvesting (31). TiO_2 is bombarded with high energy transitional metal ions, accelerated by high voltage, these ions are then injected in the lattice of the semiconductor. This process modifies the TiO_2 structure and shifts the photo-response to the visible region. (30)

6.3.4. Dye sensitization

Dye sensitization of TiO_2 structures is performed to use visible light for energy conversion. Sunlight is harvested by the dye producing excited electrons that are then injected into the conduction band of the semiconductor (32). In order to regenerate the dyes redox electrolytes, such as I_3^-/I^-, are added. The photo-produced electrons can recombine with the excited dye species. Hence, the regeneration of the dye by the redox electrolyte has to be faster than the recombination. The regeneration of the oxidized dye occurs in the order of nanoseconds, which is typically 100 times faster than the recombination reaction and widely faster than the lifetime of the oxidized dye state (30). This difference in the velocity between the electron injection and the backward reaction makes dye sensitized semiconductors promising for solar energy conversion.

6.3.5. Composite semiconductor

Another method to enhance visible light absorption for hydrogen production is to couple two semiconductors with different bang gap widths. When a large band gap semiconductor is coupled with a small gap semiconductor presenting a more negative CB level the electrons can be injected from the CB of the small gap semiconductor to the CB of the large gap semiconductor. This method allows the extension of the light spectrum that can be used for the electron promotion to the visible region, thanks to the presence of the small gap semiconductor.

A successful coupling of the two semiconductors for hydrogen production from water splitting could be achieved if the followings condition occurs:

- Semiconductors should be photo-corrosion free
- The small band gap semiconductor should be able to be excited by the visible light
- The CB of the small band gap semiconductor should be more negative than that of the large band gap semiconductor
- The CB of the small band semiconductor should be more negative than $E_{H2/H2O}$
- Electron injection should be fast and efficient

The combination of the two semiconductors satisfying the above mentioned requirements allows to reach an higher efficiency of the photo anode, enhancing the produced photo-current and consequently increase the efficiency of the device.

In this work we focus over the coupling of TiO_2 (band gap 3.2 eV) with a narrow band gap semiconductor, such as CdS (band gap 2,4 eV). CdS is a suitable candidate for the creation of a composite semiconductor because it satisfies most of the requirements, unfortunately it does not exhibit enough resistance towards the photo-corrosion.

The process of the electron-hole production is similar to dye sensitization. The difference is that the electrons are injected from one semiconductor to another semiconductor.

In our case it is probable that both the semiconductors are excited and absorb different wavelength in the solar light spectra (see Figure 10-14) under illumination, the TiO_2 in the UV part and the CdS in the near- visible part.

When the composite semiconductor is illuminated, CdS absorbing light in the near visible region allows the promotion of some electrons to its CB, leading to the formation of electron-holes pairs. Then the electrons promoted in the CB of the CdS are injected in the CB of TiO_2, while the VB holes are staying in CdS.(30) At the same time TiO_2 is absorbing the UV light producing new electron holes pairs. The injection of the latter electrons in the CB of the coupled semiconductor facilitates the electron-holes separation preventing charge recombination, Figure 6-1 presents a scheme of the process.

The CdS alone is unstable towards the photo-corrosion as a result of the S^{2-} oxidation by the photo-generated holes and the consequent release of Cd^{2+} into the solution. However, this can be hindered by performing the reaction in presence of an hole scavenger (S^{2-} or SO_3^{2-}) in the electrolyte. (25)
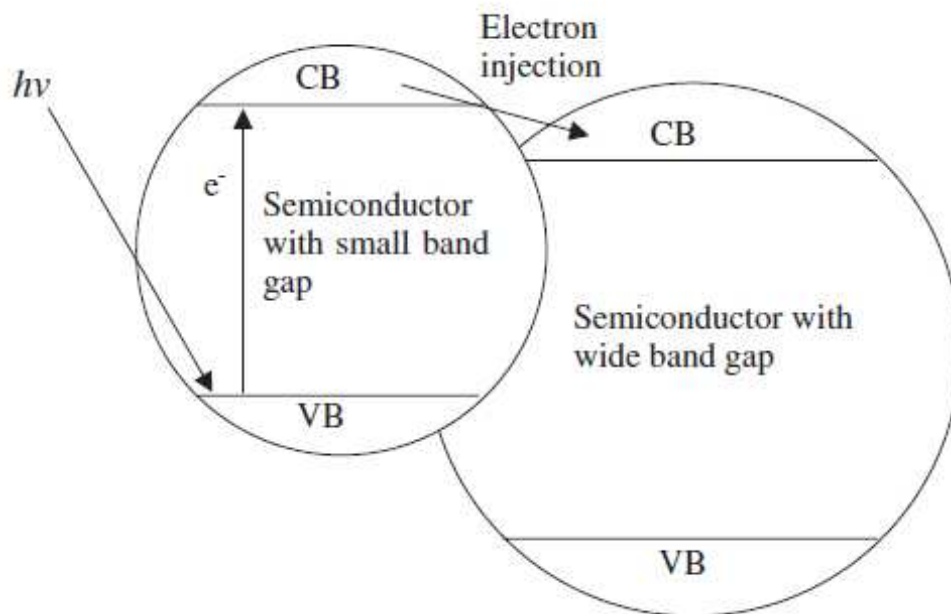

Figure 6-1 Schematic representation of the mechanism of excitation of the electrons by solar light in the case of composite semiconductors (29).

7. Efficiency of PEC cell

One key parameter for hydrogen production using photo-electrochemical technology is the efficiency of the PEC cell. The commercial potential of this kind of device will be largely determined by its costs compared to others methods of H_2 production. Increase the efficiency, and consequently minimize the energy losses, is a important step to decrease the production costs and make this technology suitable for its commercial use.

The energy losses associated with the solar energy conversion using PEC cells are associated with the following effects:

- Photons with energies lower than E_g are not absorbed, so only a limited fraction of the solar spectrum is available for the conversion.
- While photons with energy bigger than E_g are absorbed the energy exceeding E_g is dissipated as heat and therefore only a fraction of the photon energy is used in conversion.
- Only a fraction of the internal energy can be converted into chemical energy, the remaining fraction constitutes the entropy-related losses.
- There are irreversible processes associated to the recombination of electron-holes pairs, ohmic resistivity of the electrodes and the electrical connections and over potentials at the electrode electrolyte interface.

All these phenomenon contribute to the total energy losses of the PEC cell, leading to a smaller practical efficiency compared to the theoretical one.

8. Samples preparation techniques

Here are described the techniques employed for the preparation of all samples, focusing on the polyol process and the hydrothermal process used for the production of the quantum dots nanoparticles and the nanofibers respectively.

8.1.   Polyol process

The polyol process was firstly described for the preparation of finely divided metal powders of easily reducible metals (Cu), noble metals (Au, Pd) and less reducible metals (Co, Fe) by reducing inorganic precursors in liquid polyols. The polyols are either polyhydric alcohols such as 1,2-ethanediol (ethylene glycol), 1,2-propanediol (propylene glycol) or etherglycols such as di(ethylene) or tri(ethylene glycol). During the reaction the solid precursor is suspended in the liquid polyol, the solution is stirred and heated to a given temperature which can go from 0 °C until the boiling point of the solvent. The polyols are able to dissolve ionic inorganic compounds due to the presence of hydrogen bonds and high value of relative permittivity. Moreover they are mild reducing agents but this characteristic can be carried out heating the solvent up to 250°C under atmospheric pressure. Polyols can form intermediate species and absorb onto the surface of the growing particles preventing aggregation. The polyol process has been widely used for the production of oxides but adding thiourea or sodium sulphide is also possible to prepare sulphide nanoparticles.

The reaction occurs via dissolution of the solid precursors followed by the precipitation of the product from the solution. This process proceeds in two steps: nucleation and particle growth. During the nucleation step the nuclei are formed by addition of entities of the solute. In order to begin the spontaneous growth of the particles (growth step) is necessary the aggregates reach a critical size (nucleation step). The main features of the particles e.g. size, morphology, shape or degree of aggregation depend on the rates of these two steps. Numerous parameters allow to controlling these features: nature and concentration of the solid precursors, nature of the polyol, pH of the solution and the way

they are collected together, heating conditions and reaction time. In particular cases and under particular conditions is possible also to obtain nanorods or nanowires.

The formation of bulk solids and agglomerates is thermodynamically favoured over the formation of small particles with a large surface area, in order to obtain nanoparticles with narrow size and small degree of aggregation it is necessary to fulfil the following conditions: nucleation and growth must be completely separated steps and coalescence of the particles must be prevented.

Chalcogenides present low solubility in polyols, the saturation level is low and nucleation occurs as soon as the concentration of the species produced by the reduction reaction reaches a critical supersaturation level. If the product is generated slowly and the nucleation is high enough the nucleation lowers the concentration below the critical nucleation level. In these conditions the nucleation step is short and followed by the particles growth as long as the product is slowly generated and the saturation remains higher than the saturation one, Figure 8-1 (a). The nucleation rate increases quickly versus the concentration above the critical nucleation threshold, on the other hand the growth rate increases slowly above the saturation concentration Figure 8-1 (b). In order to prevent nucleation during the growth step supersaturation must remain at a low level.
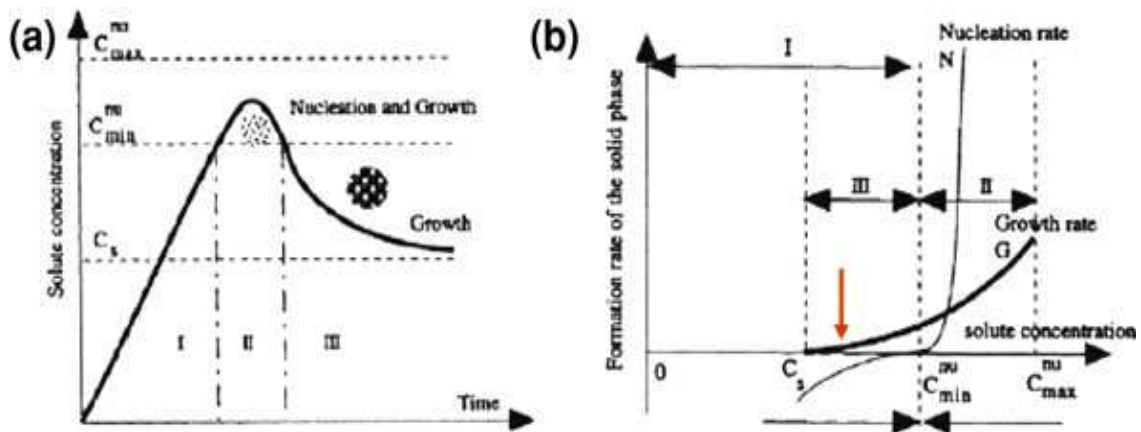

Figure 8-1 (a) Nucleation and growth (b) comparison of nucleation and growth rates versus concentration of the final compound concentration (33).

Particles growth may proceed by diffusion of the solute species over the surface of the particles and addition of atoms or ions Figure 8-2 (a), or by coalescence of particles which form larger particles Figure 8-2 (b). The second mechanism preferentially leads to an uncontrolled growth resulting into polydisperse particles of vatrious shape. Therefore it is necessary to prevent their coalescence in order to obtain particles of homogeneous shape and size. This can be achieved through steric or electrostatic stabilization. The former can be provided by the polyol itself by absorption of long chain molecules, this phenomenon can also be used to limit the size of the particles. On the other hand, electrostatic stabilization can be provided by acetate anions, when such metallic salts are used as precursors.

Whatever are the desired particles, the synthesis can be easily to performed at a laboratory scale. Interestingly, it has also been shown that the scale up the production is possible by replacing the conventional batch process by a continuous process.(33)
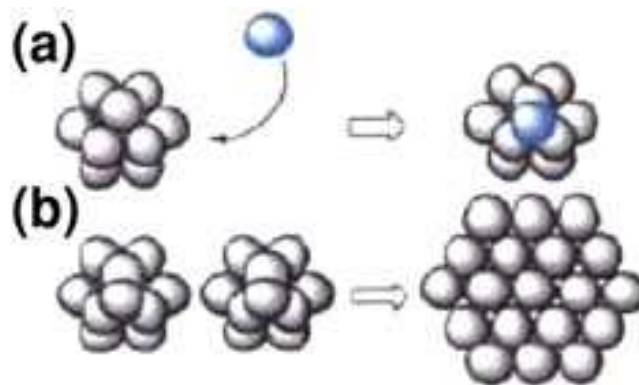

Figure 8-2 (a) Growth by addition of atoms or ions (b); growth by coalescence (33).

8.2.   Hydrothermal process

The hydrothermal technique is a multi-purpose technique for the process of advanced materials in nanotechnology. This technique was firstly used to produce artificial single-crystals and later its employment was extended to a wide variety of application fields such as: crystal growth, production of advanced materials, waste treatment, etc. Concerning the preparation of nanostructured materials it can be used not only to produce monodispersed and highly homogeneous nanoparticles but also nanotubes and nanofibers. Hydrothermal reactions can be defined as any heterogeneous reaction in presence of aqueous solvents under high pressure and temperature, allowing the dissolution and the recrystallizion of materials that are insoluble under usual conditions. (34) This method allows to produce nanostructures exhibiting high crystallinity, low dimensions and high purity through a one step process in a tightly closed vessel and it has been extensively studied owing to its cost-effective and easy route to obtain nanotubes. Considering that it is also suitable for a large scale production the technique has gained a large interest into the scientific community.

Figure 8-3 Example of autoclave used for hydrothermal treatment (34).

In the hydrothermal treatment a precursor (Ti metallic, anatase or amorphous TiO_2) is dived into an alkali solution (normally NaOH) in a tightly closed container, Figure 8-3 shows an example of autoclaves used for hydrothermal treatment. The container is heated at a given temperature and for a prefixed time. The main factors influencing the morphology and the structure of the nanotubes during the hydrothermal treatment are: the applied temperature, the treatment time, the type of alkali solution, the filling fraction of the autoclave and the precursor. In order to obtain the desired phase and a stable structure with a large crystalline content, the samples produced by hydrothermal route are later processed by acid washing and thermally treated. However the as- produced structures do not show photocatalytic activities probably because the the TiO_2 is not very well crystallized. Hence a thermal treatment was carrid out in a range of temperatures between 300 °C and 700 °C, overstep this temperature leads to the formation of rutile phase which is not suitable for the intended application. This last production step helps the formation and the stabilization of the anatase nanofibers.

Many studies have attempted to understand and explain the structure and the formation mechanism of the TiO_2 nanorods produced by hydrothermal method but they are still ambiguous (35).

The mains disadvantages of the hydrothermal method are the long duration of the synthesis, the difficulties in achieving uniform size and a preferential alignment of produced structures and the need to add highly concentrated NaOH solution. Some methods have been developed to enhance the formation of nanotubes and shorten the duration of the synthesis such as sonication or microwave irradiation during the treatment, but in this case the risk is to destroy the structures (35).

9. Samples preparation

In this chapter the methods employed for the production of the samples are briefly described. Some process details, such as precise quantities of the reagents used or concentration of the solutions employed, are omitted in order to preserve the laboratory know-how. Few papers are in preparation. The chapter is organized in three sections representative of the three main steps of the nanocomposite synthesis: CdS QDs synthesis, TiO$_2$ NFs synthesis, CdS/TiO$_2$ nanocomposite synthesis.

9.1.   *CdS quantum dots synthesis (QDs)*

The QDs were produced using the polyol process. In a three necks round-bottom flask were added the metallic precursor (Cadmium acetate), the sulfur agent (thiourea), the surfactant (TOPO trioctylphosphine oxide) and the solvent (DEG diethyleneglycol). The reaction was carried out dissolving in 80 ml of solvent (DEG): $4x10^{-4}$ mole of the metallic precursor (Cadmium acetate) and $4x10^{-4}$ mole of surfactant (TOPO) and an excess of thiourea. All the quantities of reagents used in this reaction are presented in Table 9-1. On the top of flask were prepared a condenser, a mechanic stirrer and a thermocouple. The solution was heated until 180 °C with a fixed heating ramp of 6 °C/min and maintained at 180 °C for 30 minutes. Then the heating was stopped and the mixture was cooled down until room temperature (RT). During all the process the solution was mechanically stirred (Figure 9-1). The product was recovered as a suspension of CdS QDs in DEG (Figure 9-2). Before any characterization, one can recognize the characteristic yellow color of the CdS QDs.

Table 9-1 calculated and measured quantities of the reagents of the polyol reaction

	Cadmium acetate	Thiourea	TOPO (surfactant)
Calculated quantity [g]	0,132(9)	0,045(6)	0,193(0)
Measured quantity [g]	0,133(0)	0,046(0)	0,193(0)

(a) (b)

Figure 9-1 Polyol experimental procedure used for the CdS production by polyol process (a) during the heating step and (b) during the cooling step.

Figure 9-2 Suspension of CdS quantum dots in polyol (DEG).

9.2.   TiO₂ nanofibers synthesis (NFs)

The TiO$_2$ nanofibers were produced by corrosion of Ti sheets. The sheets (0,9x2 cm) were firstly chemically polished. The polishing consists: a first treatment was performed by sonication in ethanol absolute followed by a cleaning in oxalic acid solution (5 wt-%) at 100 °C for 2 h, then rinsed with deionised water and dried. This cleaning step is important for the further nanofiber growth step, allowing to eliminate all the dirt and the oxides present on the surface of the Ti and obtaining a clean surface suitable for the following production steps. Hydrothermal synthesis was carried out using in a stainless steel Teflon lined autoclave (Figure 9-3), the Ti sheets were dived in a H$_2$O$_2$ - NaOH solution inside the autoclave. All volumes and the concentrations of the solutions are presented in Table 9-2. Then, the autoclave was put in the oven at 80°C for 24 h in order to start the hydrothermal synthesis and then cooled down until RT. Afterwards the Ti/TiO$_2$ sheets have been rinsed and dried. Later they were subjected to post treatments: acid washing and calcination. The acid washing was conducted through two cycles in 50 ml of low concentrated (0.1M) HCl solution for 2 hours each time. Finally the sheets were dried and thermally treated at 400 °C for 1 hour.

Table 9-2 Volume of the reagents used for the hydrothermal reaction

	Hydrogen peroxide (H$_2$O$_2$ 30 wt-%)	Sodium hydroxide (NaOH 10 M)
Volume [ml]	15	15

Figure 9-4 presents a Ti sheet before (a) and after (b) the hydrothermal treatment. Once can notice the white layer over the metallic surface induced by the hydrothermal process and attributed to the presence of TiO$_2$.

Figure 9-3 Autoclave used for the hydrothermal process.

(a)

(b)

Figure 9-4 Ti Sheet (a) before and (b) after the hydrothermal treatment.

9.3. TiO$_2$/CdS nanocomposite synthesis

TiO$_2$/CdS nanocomposites were synthesized by impregnation of the CdS QDs over the surface of TiO$_2$ NFs. The Ti/TiO$_2$ sheets were plunged in 5 ml CdS QDs suspension. Afterwards the sheets were left in the in the solution for 21 h. Finally the samples were recovered after washing and drying. Figure 9-5 presents a Ti/TiO$_2$ sheet at the end of the procedure.
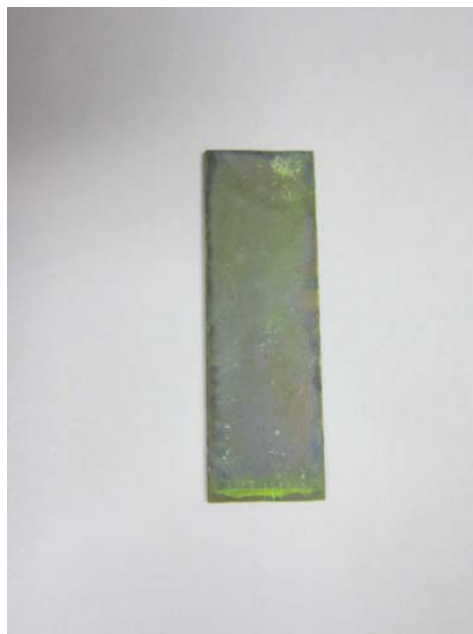
Figure 9-5 Sample after impregnation.

10. Characterization

The samples were characterized in order to determine the chemical composition, the morphology and of the produced structures were the expected ones. Here following I am presenting the characterization techniques and the instruments used. Then, the presentation of my results is organised in three parts, reflecting the order of the production steps of the nanocomposites: CdS quantum dots (QDs), TiO_2 nanofibers (NFs) and the CdS/TiO_2 nanocomposites.

10.1. Characterization techniques and instruments

First, the structures (CdS, TiO_2) were characterized by X ray diffraction (XRD) using a Panalytical Empyrean equipped with a multichannel detector (PIXcell 3D) using a Cu-Kα radiation in the 20-90°=2θ range.

The morphology of the CdS nanoparticles was analysed using a transmission electron microscope (TEM) performed on a JEOL 21000F microscope operating a 200kV. The particle size was obtained from the recorded TEM images and further analyses with SAISM software (Microvision Instruments) calculating the average particle diameter through a statistical analysis counting about 200 particles considered to be spherical.

The UV-Visible spectrum of the polyol-CdS suspension was recorded on a CARY 56^E spectrometer in transmission mode.

The microstructure of the TiO_2 NFs and the TiO_2/CdS composites was studied using a Supra40 ZEISS field emission gun scanning microscope (FEG-SEM) operating at 2,5 kV. UV-Visible diffuse reflectance spectra of TiO_2 and TiO_2/CdS composite were registered on a Perkin Elmer –Lambda 1050 spectrophotometer equipped with a PTFE-coated integration sphere.

X-ray photoelectron spectroscopy (XPS) analysis was performed the Ti/TiO_2 sheets before and after impregnation. The device used was Thermo VG ESCALAB 250 equipped with micro-focused, monochromatic Al Kα X-ray source (1486,6 eV) and magnetic lens. The X-ray spot size was   500 μm (15 kW, 150 W). The spectra were obtained in constant analyzer energy with pass energy of 150 and 40 eV for the general

spectra and the narrow scan respectively. The samples were fixed to the on the samples holders with conductive adhesive tape and degassed for 5 h at 2×10^{-7} bar. The Avantage software was used for data acquisition and processing.

10.2. Results

10.2.1. CdS quantum dots (QDs)

The shape of the as produced CdS QDs was analyzed using TEM microscopy (Figure 10-1). The pictures, recorded analyzing a drop of polyol based colloid containing CdS nano particles, show a collection of spherical nanoparticles, their diameter was evaluated by image analysis. Figure 10-2 shows the size distribution of the particles, the average diameter has been found to be about 3.6 nm with a standard deviation of 0.6 nm.
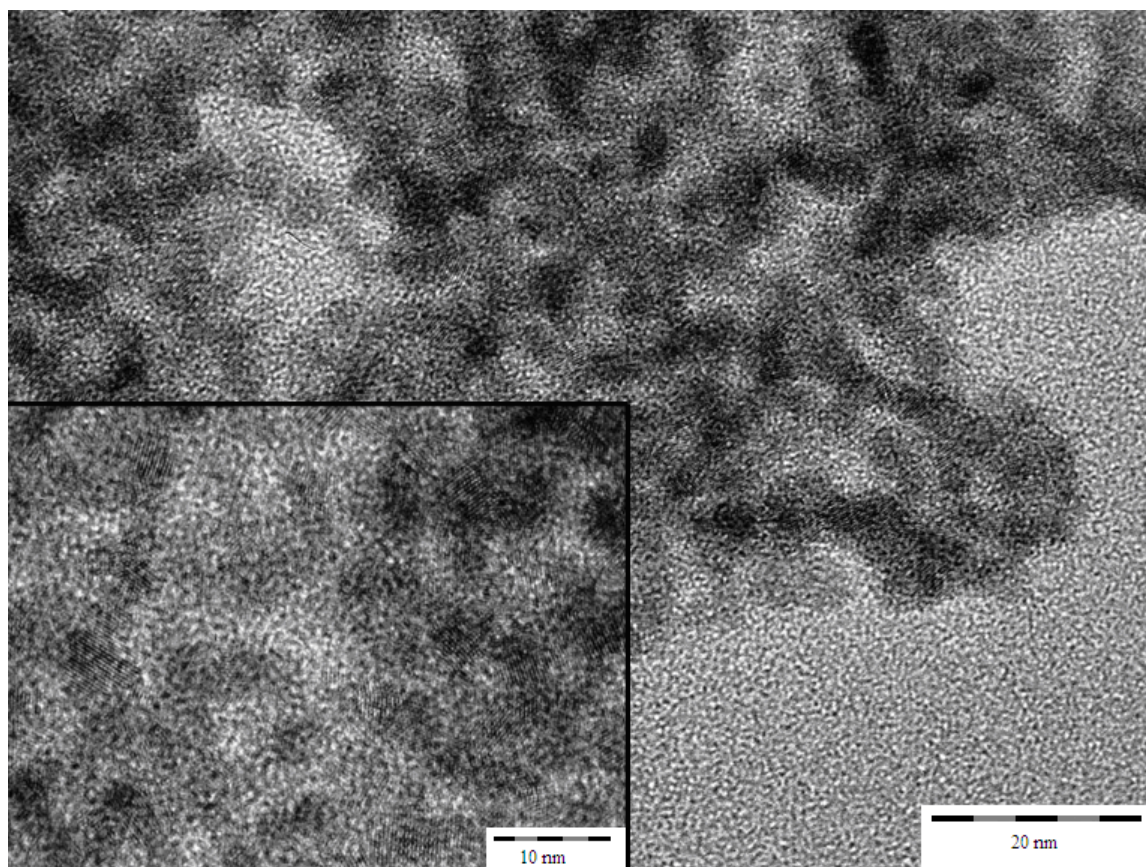
Figure 10-1 TEM image of the as produced CdS QDs with different magnifications.
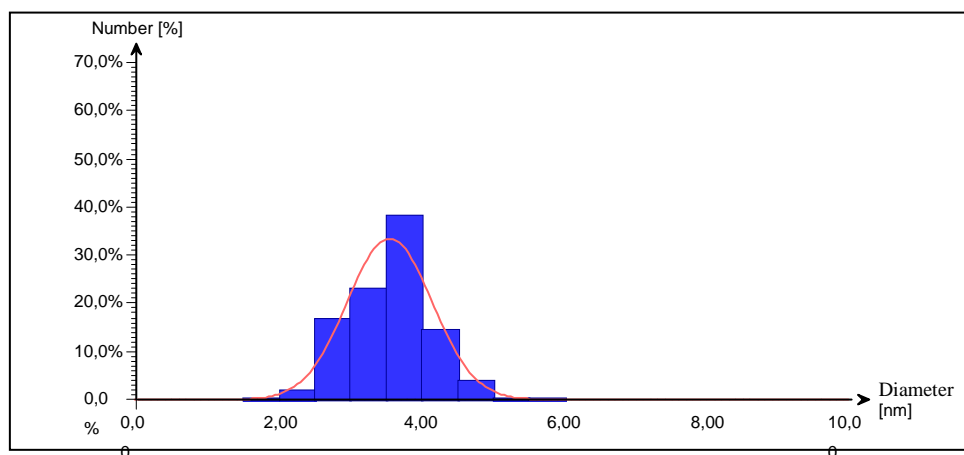
Figure 10-2 Size distribution histogram of the as produced CdS QDs.

Table 10-1 Results of the CdS QDs size evaluation.

Average diameter [nm]	Standard deviation [nm]
3,6	0,6

The XRD powder diagram of CdS (Figure 10-3) presents all the characteristics CdS cubic phase peaks. It is possible to recognize the (111) plane peak at 26°, the (220) plane at 44° and the (311) plane at 51°. Therefore, the crystal structure of the prepared CdS is assumed to be cubic (36). The recorded XRD plot presents larges peaks, that means small crystalls inside the particles. As in shown in TEM pictures and in dimension analysis the nanoparticles are small (average diameter about 3.6 nm) it is possible to assume that the nanoparticles are monocrystalline.
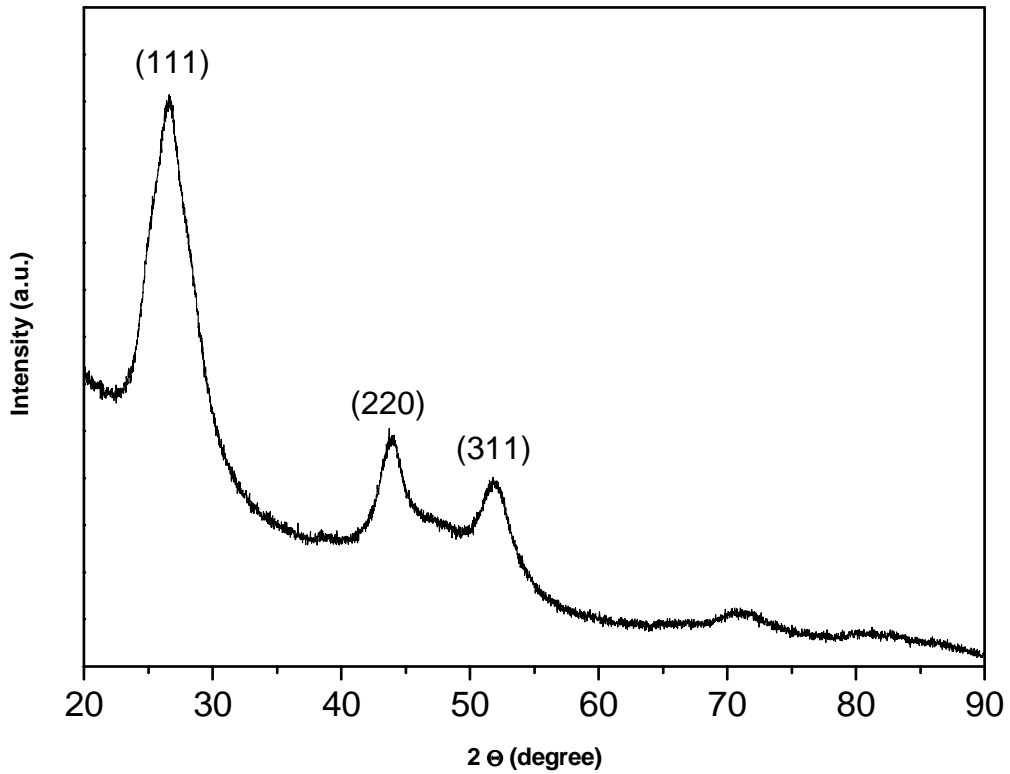
Figure 10-3 XRD pattern of as produced CdS QDs.

The value of the energy gap was then determined from the Uv-Visible absorption spectrum measuring the absorbance of homogeneously dispersed CdS nanoparticles and subtracting the absorbance of the reference solution (DEG without particles). The data recorded were plotted using the Tauc rappresentation and are presented in Figure 10-4.

The direct band gap E_g coresponds to the intersection point of the extrapoled straight line portion of the curve $(h\alpha\upsilon)^2$ as function of $h\upsilon$, with the abscissa axis: where $h\upsilon$ is the photon energy and α measure the absorbtion coefficent, α was calculated from the Lambert-Beer relation:

$$\alpha = 2{,}303\frac{A}{d} \qquad (1)$$

Where d is the path length of the quarz cuve (1 mm) and A is the absorbance. The band gap found was 3,22 eV. This value is in good agreement with the value calculated from the Bruss equation (2): E_g= 3,1 eV. (37)

$$E_g = E_g^{bulk} + \frac{\hbar^2 \pi^2}{2R^2}\left(\frac{1}{m_e^*} + \frac{1}{m_h^*}\right) - \frac{1,8e^2}{4\pi\varepsilon R} \quad (2)$$

Where R is the particles radius (1.8 nm), m_e* = 0.19 m_e is the effective mass of the electron, m_h*= 0.8 m_e is the effective mass of the hole, m_e is the mass of the electron, ε is the dielectric constant of the material and E_g^{bulk} is the bulk energy gap (2.42 eV) (38).

One can notice the difference between the experimental E_g value (3.22 eV) mesured for the particles and the bulk value E_g^{bulk} (2.42 eV). Indeed, particles whose dimensions become of the order of magnitude of bulk exciton Bohr radius (for the CdS ≈ 3 nm (38)) exhibit quantum confinement effect, this results in the dependence of the E_g value by the particles size. The decrease the QDs size leads to increase the width of the band gap E_g. Confinement effects can be strong for particles presenting radius significantly smaller than the Bohr radius of the bulk exciton. The main consequence results in a shift of the absorption edge to lower values of the wavelength (blue shift) due to an increase in the energy band gap.
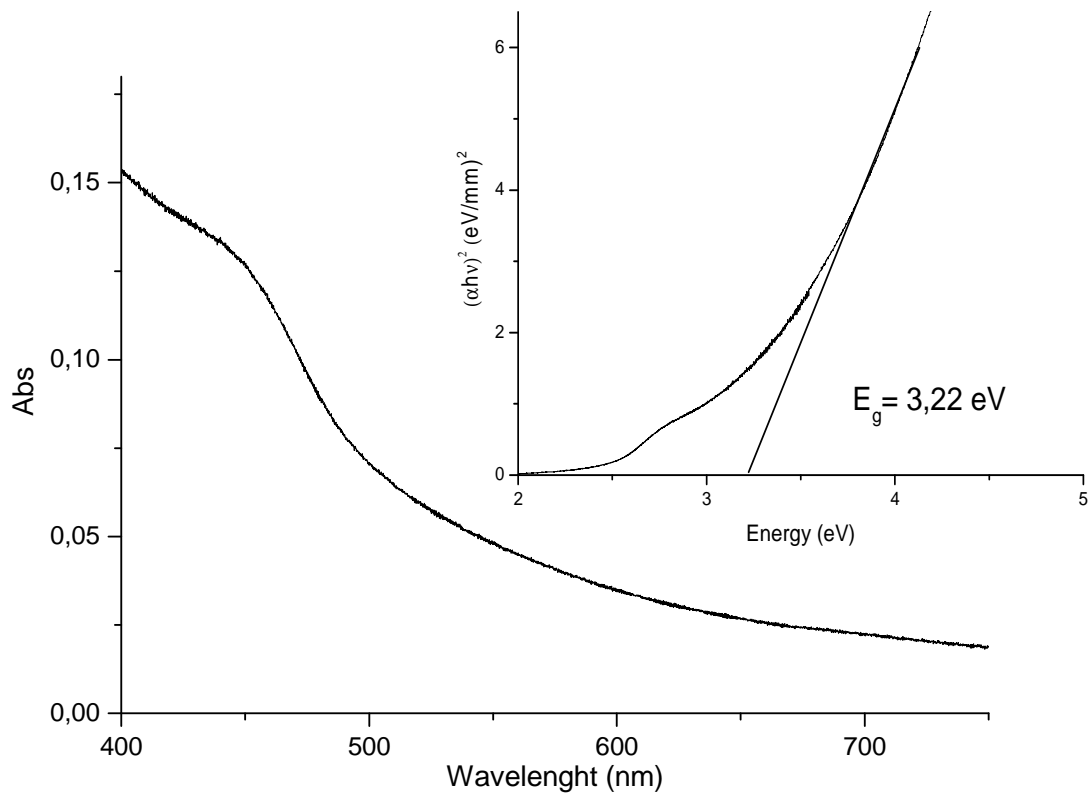
Figure 10-4 UV-Visible spectra and band gap determination of CdS quantum dots.

10.2.2. TiO$_2$ nanofibers (NFs)

Figure 10-5 (a) and (b) show SEM images of the surface of Ti sheets after hydrothermal treatment with two different magnifications. One can notice that we have obtained a complex and homogeneous structure made up of branched TiO$_2$ nanofibers. The porosity offered by such structure is a good feature which permits to easily include the CdS QDs during the further impregnation treatment. Moreover, the high surface to volume ratio of this structure allows a wider surface contact between the TiO$_2$ and the CdS and hence a higher active surface for the H$_2$ production enhancing the efficiency of the device.

1 µm
EHT = 2.50 kV   WD = 5.0 mm   Signal A = InLens
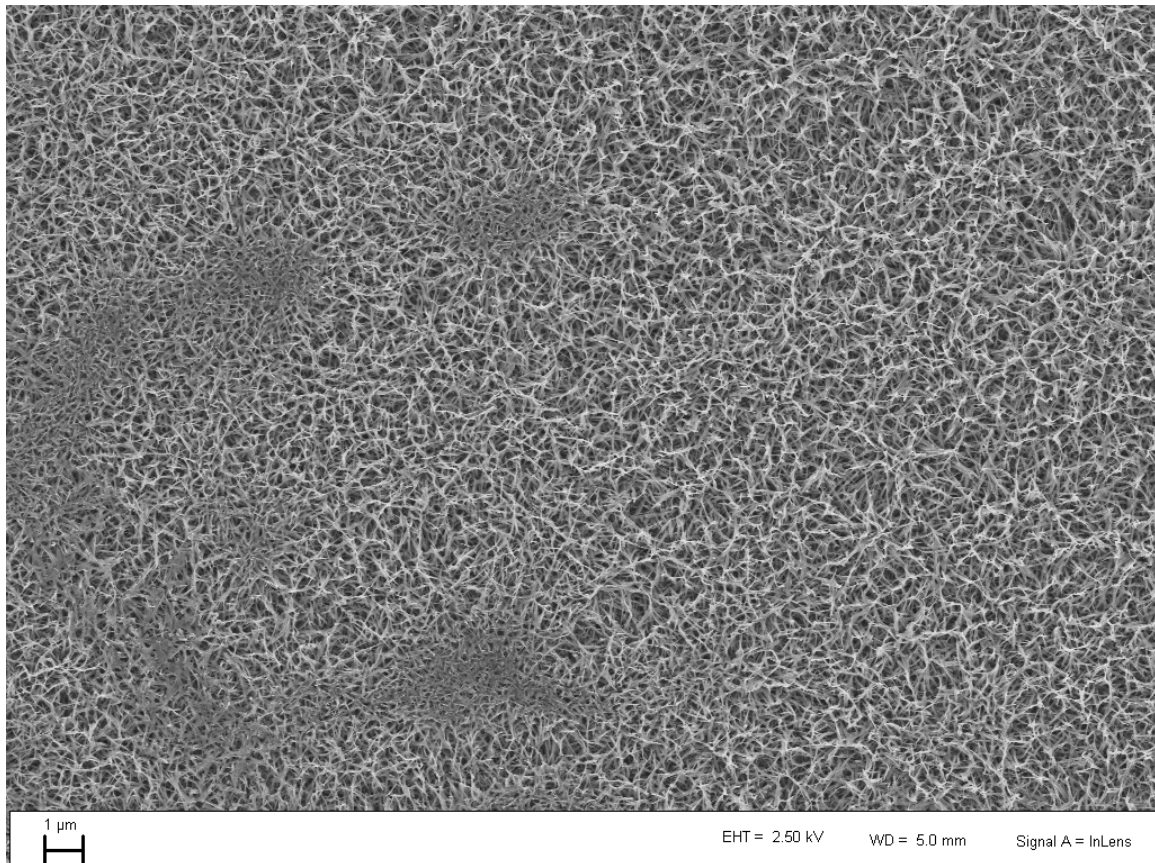
(a)
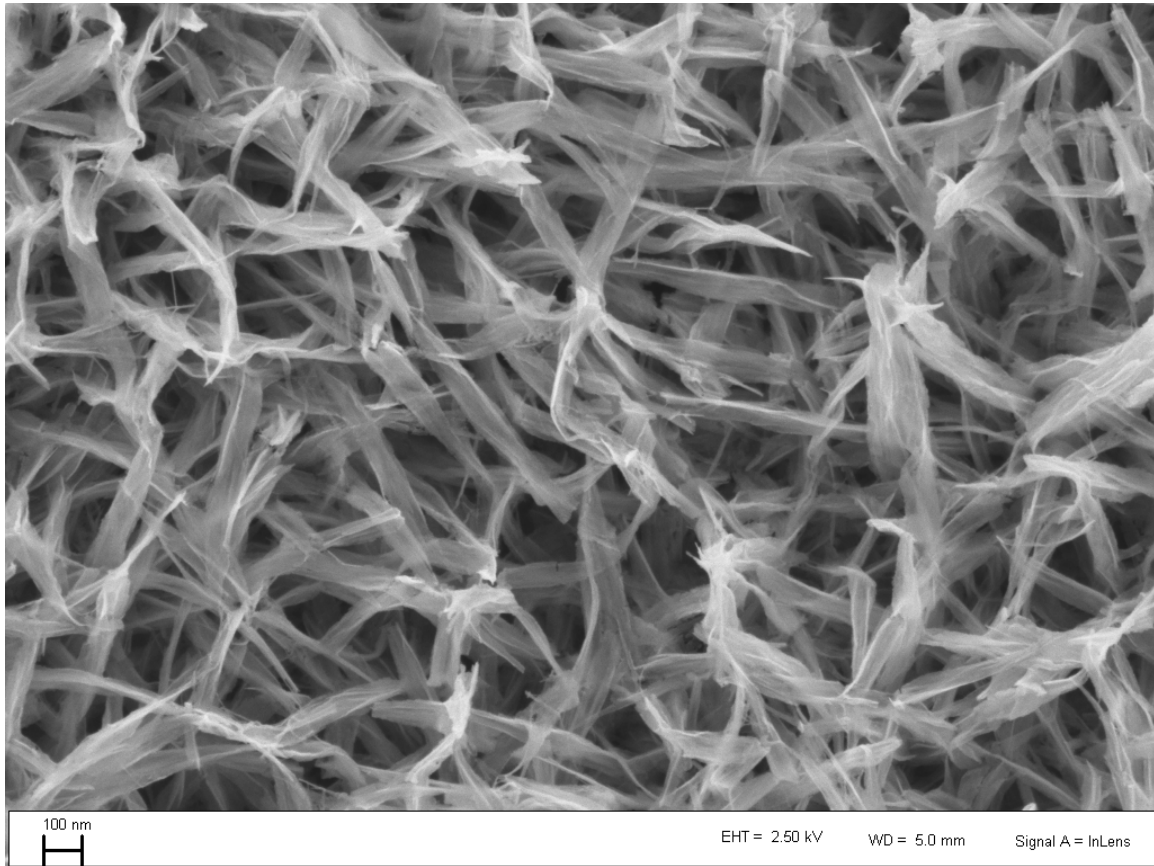
(b)

Figure 10-5 SEM pictures of the TiO$_2$ nanofibers surface scale bar (a) 1µm and (b) 100µm.

Figure 10-6 and Figure 10-7 were obtained embedding the samples produced via hydrothermal treatment into a polymeric resin. Then these samples were scratched out until the emersion of the sample's cross section from the resin (microtomy), then covered by a carbon powder in order to perform the observations by SEM.

Figure 10-6 depicts a SEM image cross-section of the TiO$_2$ layer and a measure of its thickness by image analysis. Here it is possible to see the resin layer, the black surface, the Ti layer, the light grey surface, and between them the TiO$_2$ layer. One can notice that the TiO$_2$ layer has not a uniform thickness and present a large porosity. The average thickness value obtained from image analysis was found to be about 16,43 µm.
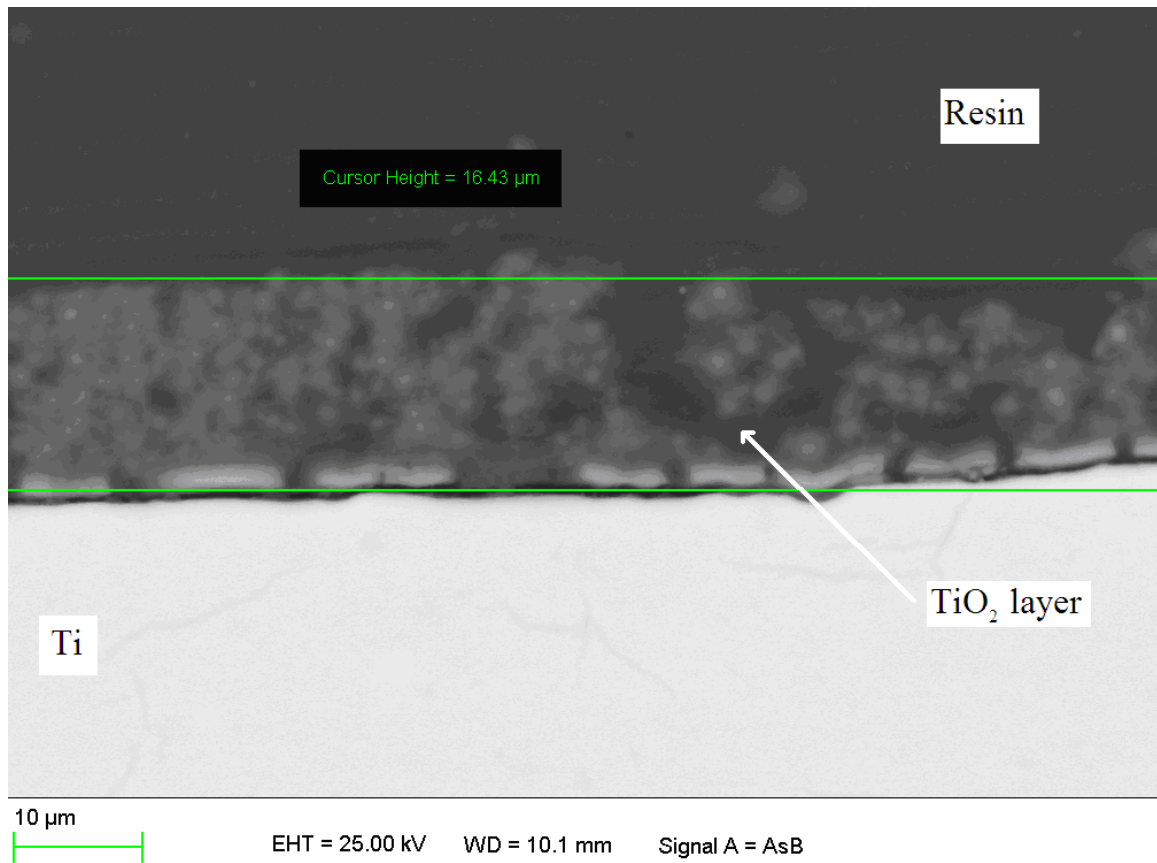
Resin

Cursor Height = 16.43 µm

TiO$_2$ layer

Ti

10 µm

EHT = 25.00 kV   WD = 10.1 mm   Signal A = AsB

Figure 10-6 SEM image of the produced TiO$_2$ layer and thickness determination by image analysis.

Figure 10-7 presentsa SEM image of the TiO$_2$ layer with higher magnification we can clearly observe the high porosity of the TiO$_2$ layer.
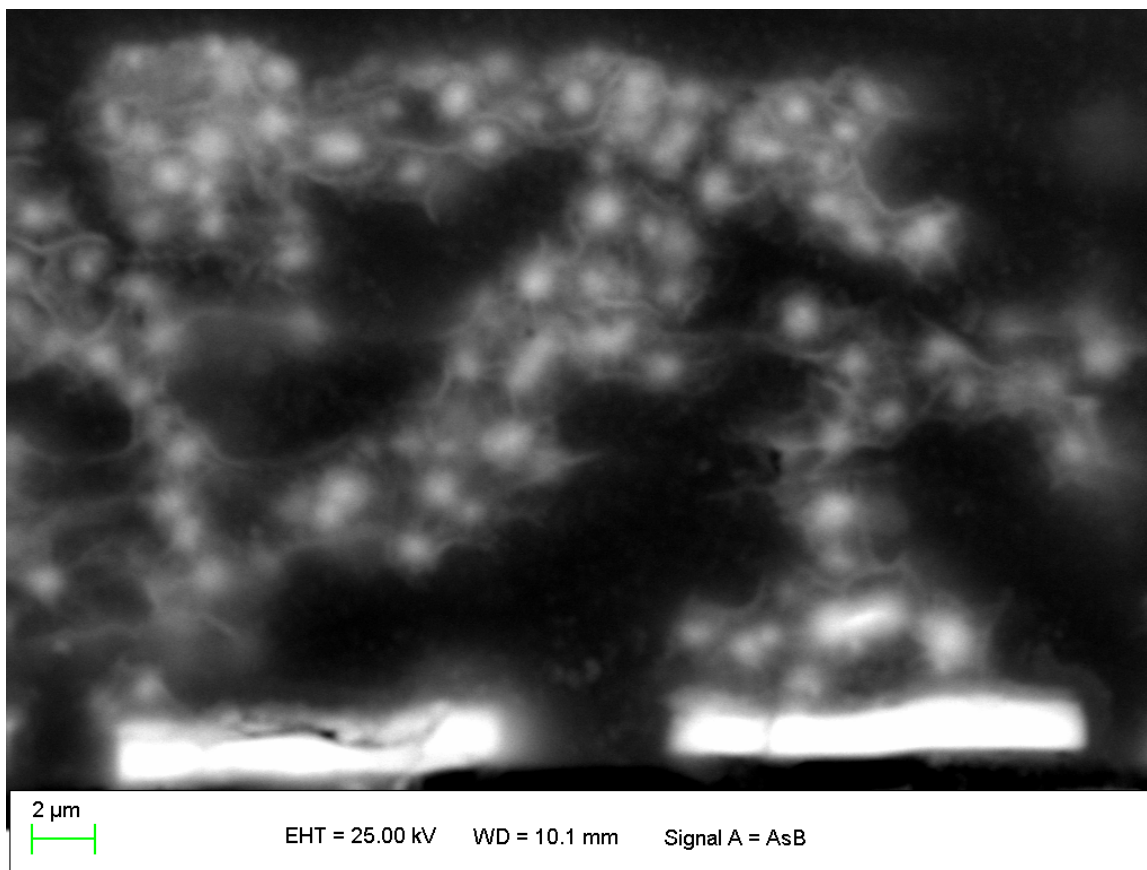
Figure 10-7 SEM image of the TiO₂ layer.

The presence of crystalline TiO_2 is confirmed by the X-ray diffraction XRD analysis (Figure 10-8) the pattern clearly shows the peaks at 25° and 48° characteristics of the TiO_2 anatase phase whereas other strong peaks 38° and 40° can be assigned to the metallic Ti substrate. The anatase peaks are slightly wider than the metal peaks, confirming the formation of small oxide phase crystals during the hydrothermal treatment.
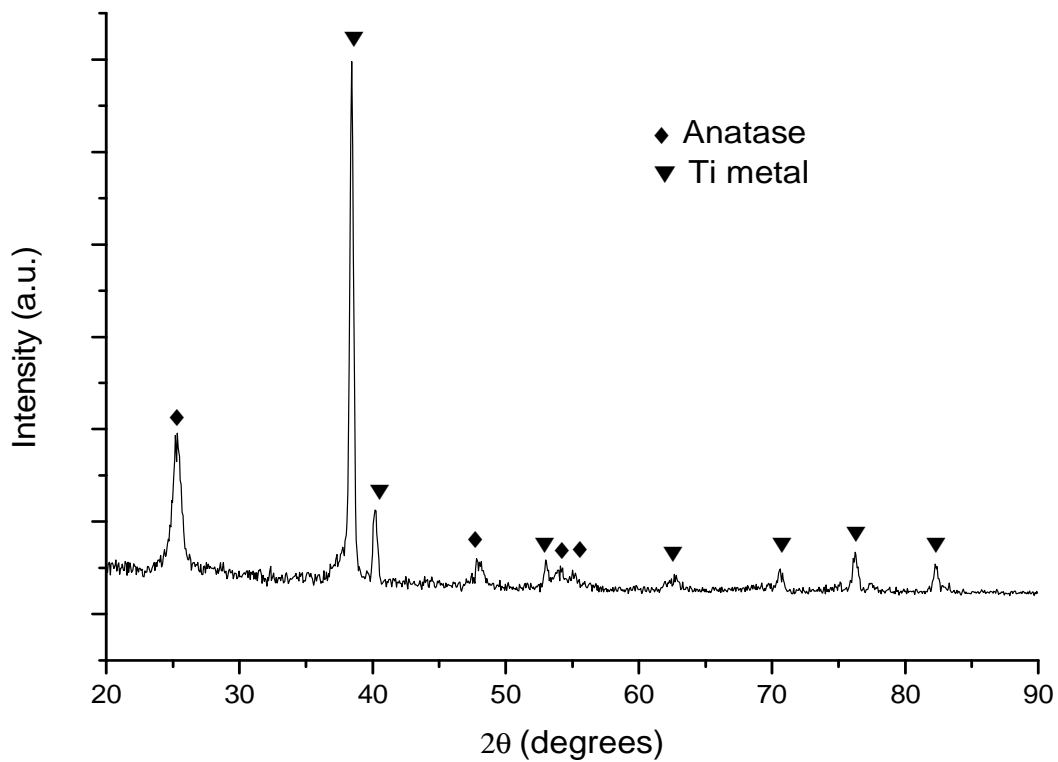
Figure 10-8 XRD pattern of the Ti/TiO₂ sheet before impregnation.

The band gap energy (E_g) was evaluated from the data collected from Uv-Visible diffuse reflectance spectroscopy (Figure 10-9). The results were analysed using the Kubelka-Munk method based on the following equation:

$$F(R) = \frac{(1-R)^2}{2R}$$

where R is the reflectance and F(R) is proportional to the extinction coefficient α. Kubela-Munk function can be obtained as following:

$$(F(R)h\upsilon)^n$$

where n is a coefficient associated with an electronic transition, in our case we used n=1/2 that corresponds to an allowed transition (39).

The E_g was calculated plotting a $(F(R)h\upsilon)^{1/2}$ as function of $h\upsilon$ and extrapolating the straight line to the abscissa axis. We obtained is 3.32 eV very close to the bulk value 3,2 eV.
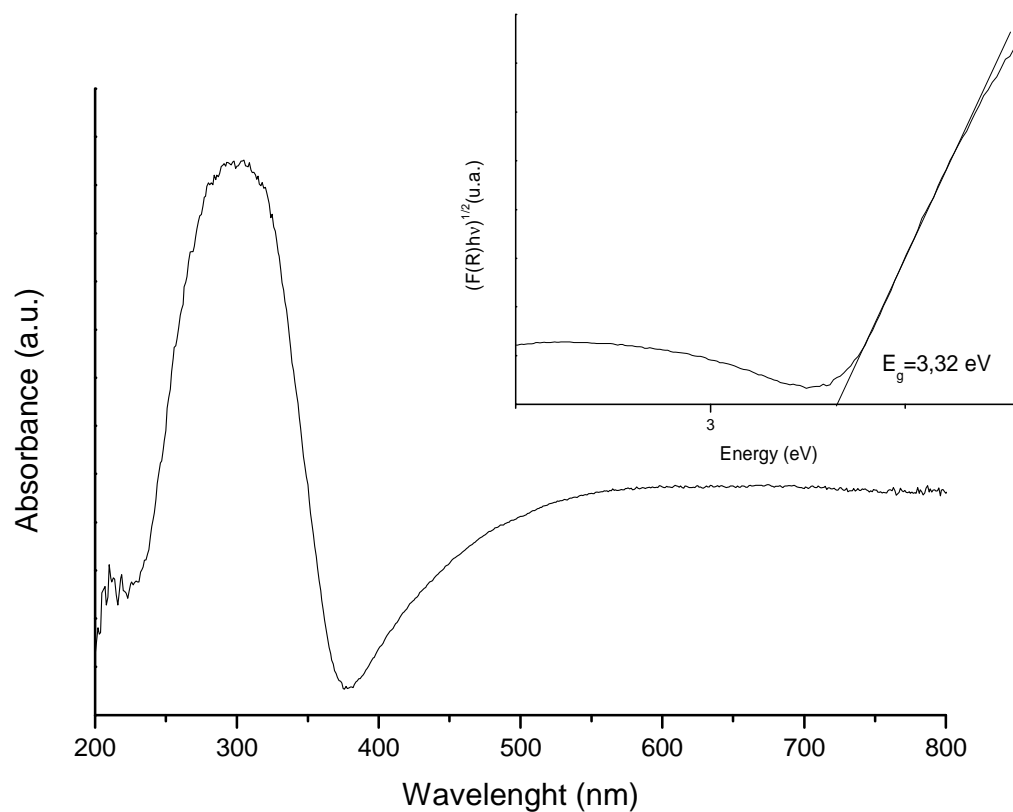

Figure 10-9 UV-Visible spectra of TiO₂ nanostructures and determination of the bad gap of TiO₂ nanofibers.

10.2.3. TiO$_2$/CdS nanocomposite

After impregnation, the composites were analyzed in order to evidence the presence of the CdS nanoparticles at the surface of TiO$_2$ nanofibres. A SEM image of the developed morphology obtained is shown in Figure 10-10 (a) and (b). One can notice the differences between the nanofibres before (a) and after (b) impregnation. After the treatment the fibre's surface appears to be rougher and covered by a layer of CdS particles, due to their small size it is difficult to characterize the interaction between CdS nanoparticles and TiO$_2$ nanofibres. They may likely cover the nanofibres individually and also fill the pores of the TiO$_2$ substrate or form multiple layers over the fibres surface.


100 nm   EHT = 2.50 kV   WD = 5.0 mm   Signal A = InLens
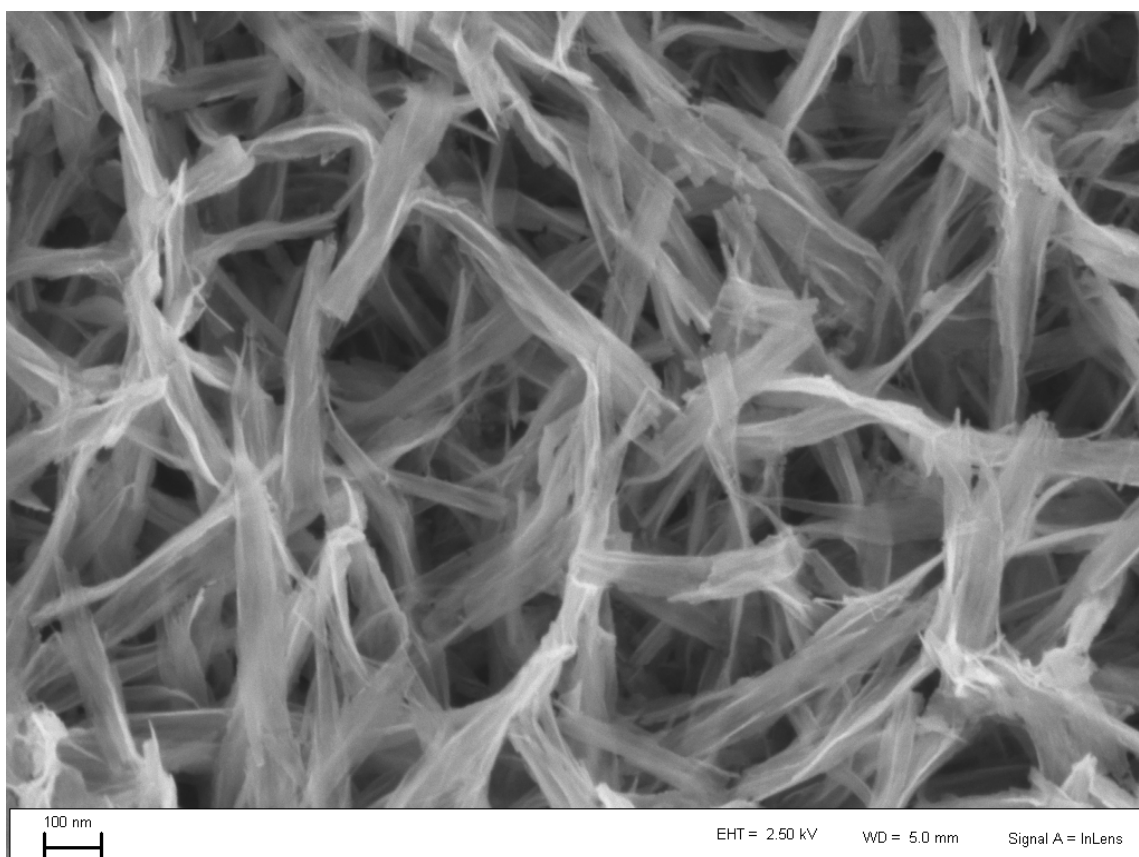
(a)
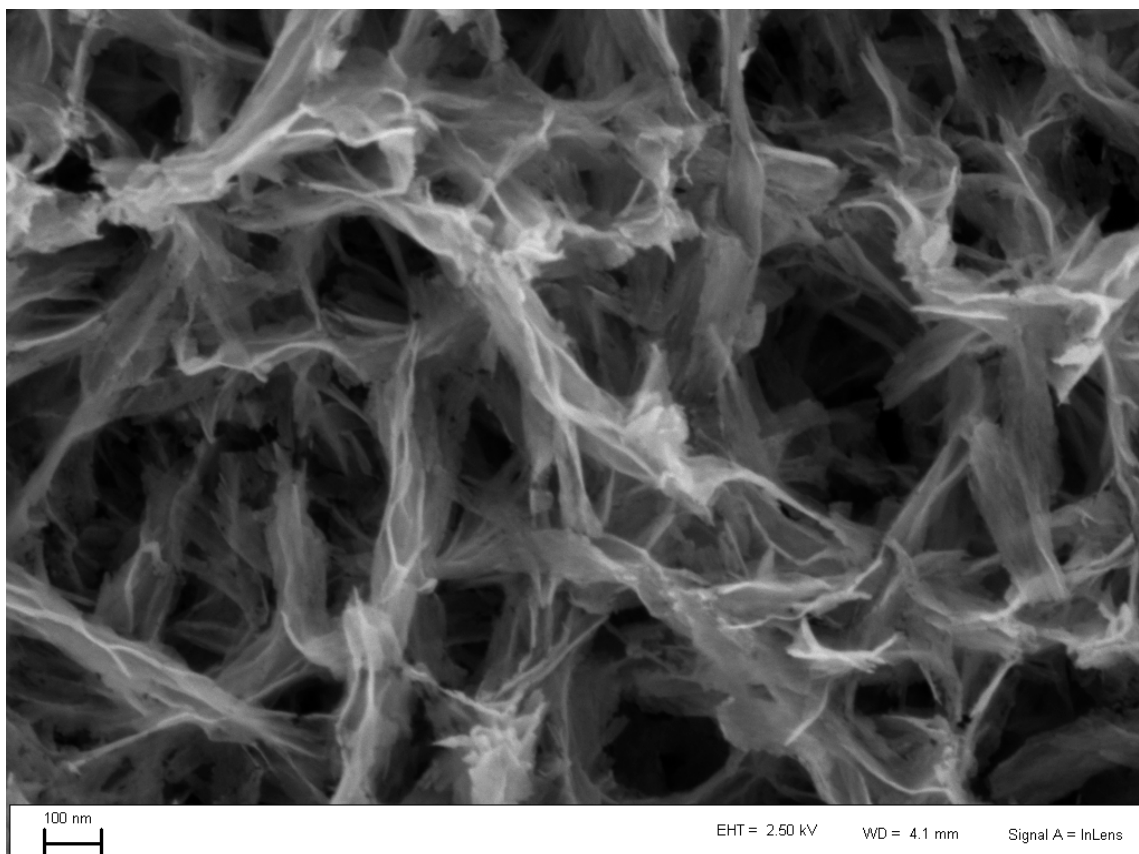
(b)

Figure 10-10 SEM images of the surface before impregnation (a) and after (b).

HRTEM images have been performed after peeling off the fibres from Ti/TiO$_2$ substrate before (a) and after (b) impregnation. (Figure 10-11) (a). The comparison between both two images led to the conclusion that a good adhesion was achieved between the particles and the fibres. This result is very important, particularly because a good contact between both components allows a good electron transfer through semiconductors.

(a)

TiO$_2$ NF

CdS QDs
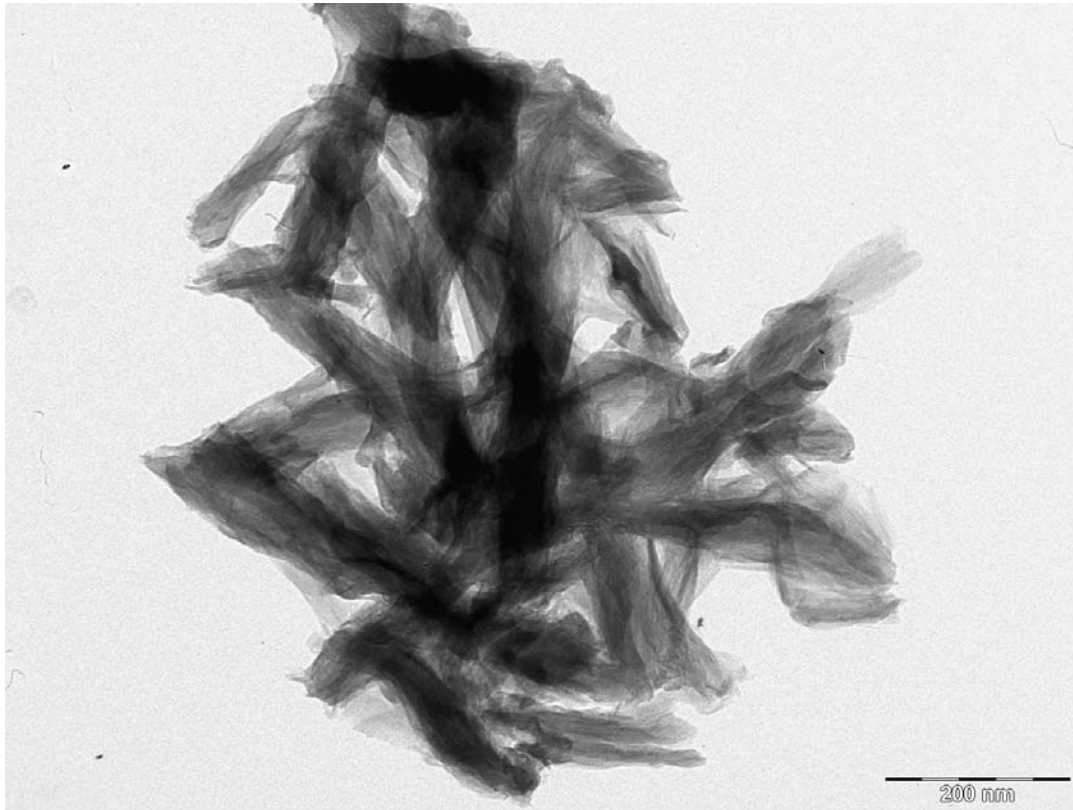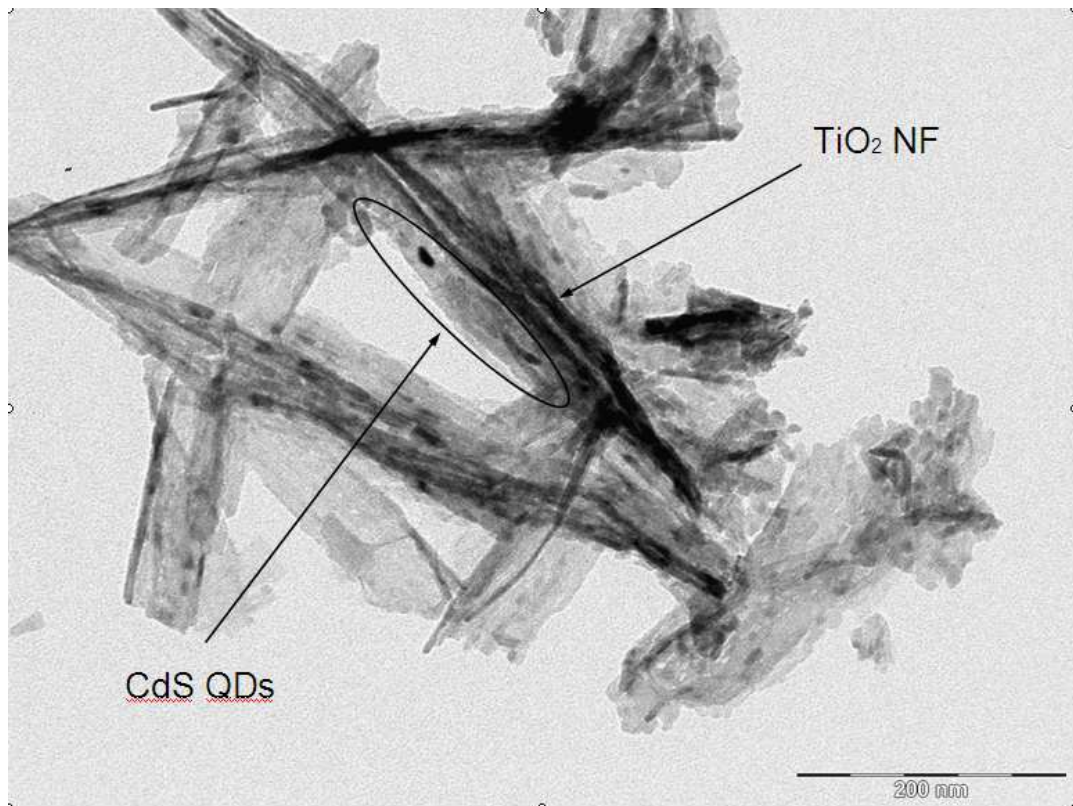
(b)

Figure 10-11 HRTEM images of the fibers before (a) and after (b) impregnation.

XRD analysis has been performed on the impregnated fibres layer but the CdS peaks could not been detected, this is due to their small size. In θ- θ Bragg-Brentano diffraction configuration for the working $2\theta= 20$-$90°$ range the X-ray beam penetration depth is much larger than the grain size of the QDs deposed over the surface of the Ti/TiO_2 bulk material. Therefore the presence of a thin layer of CdS may escape from this analysis.

To confirm the presence of a CdS layer over the TiO_2 the sample was studied by X-ray photoelectron spectroscopy XPS, a low resolution spectrum with large scale energy is presented in Figure 10-12. The high resolution XPS spectra for the TiO_2/CdS sample is shown in Figure 10-13 here is possible to easily recognize the Ti2p (a), Cd3d (b), O1s (c) and S2p (d) peaks. The $Ti2p_{3/2}$ and $Ti2p_{1/2}$ at 459 eV and 465 eV respectively correspond to Ti^{4+} in tetragonal structure. There are no evidence of Ti^0 species peaks, this suggest that the depth of the XPS analysis is smaller than the TiO_2 layer.

The O1s spectrum shows a narrow peak at 530 eV imputable to the Ti-O bond in TiO_2. The $Cd3d_{5/2}$ and $Cd3d_{3/2}$ peaks at 406 eV and 412 eV can be assigned to Cd^{2+} in CdS nanoparticle. Finally the S2p signal is split into two components: at 162 eV corresponding to S^{2-} of the CdS and 169 eV corresponding to the oxidized form SO_4^{2-} .This suggest that the surface of CdS QDs is oxidized. These results confirm that the samples are composed of TiO_2 and CdS and that QDs are probably sligtly oxidized on the surface.
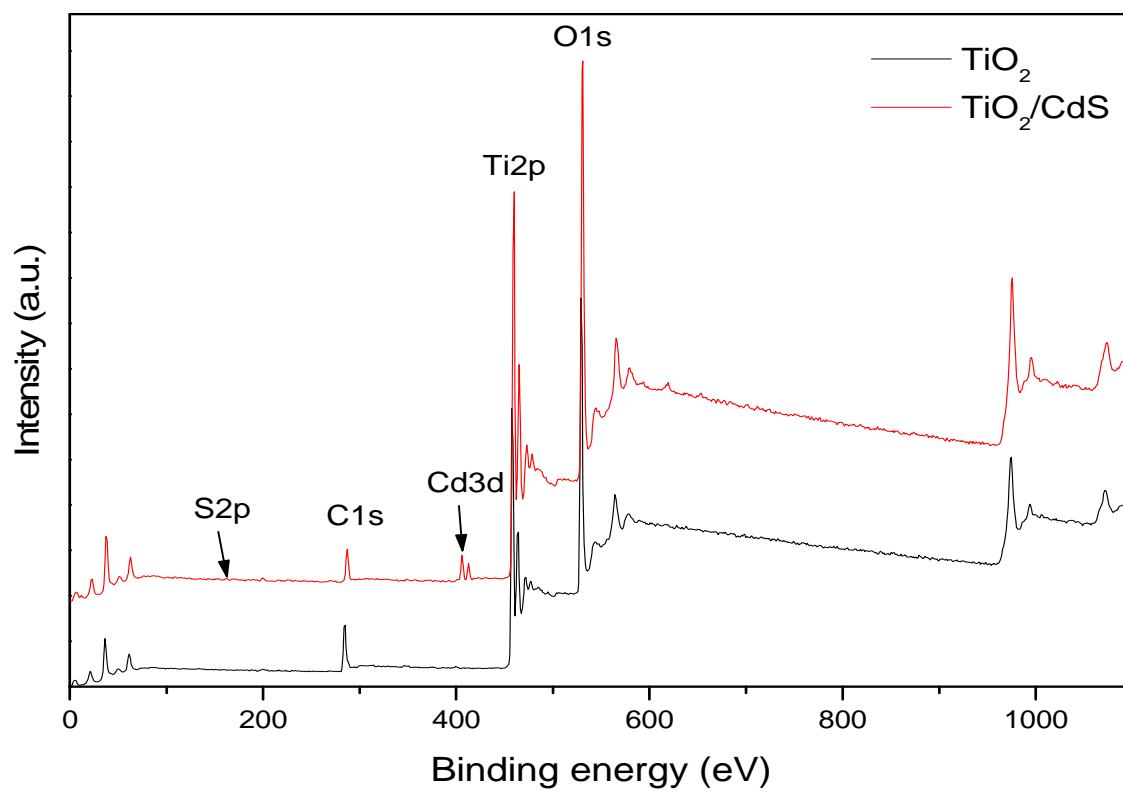
Figure 10-12 XPS spectra of the samples before and after impregnation.
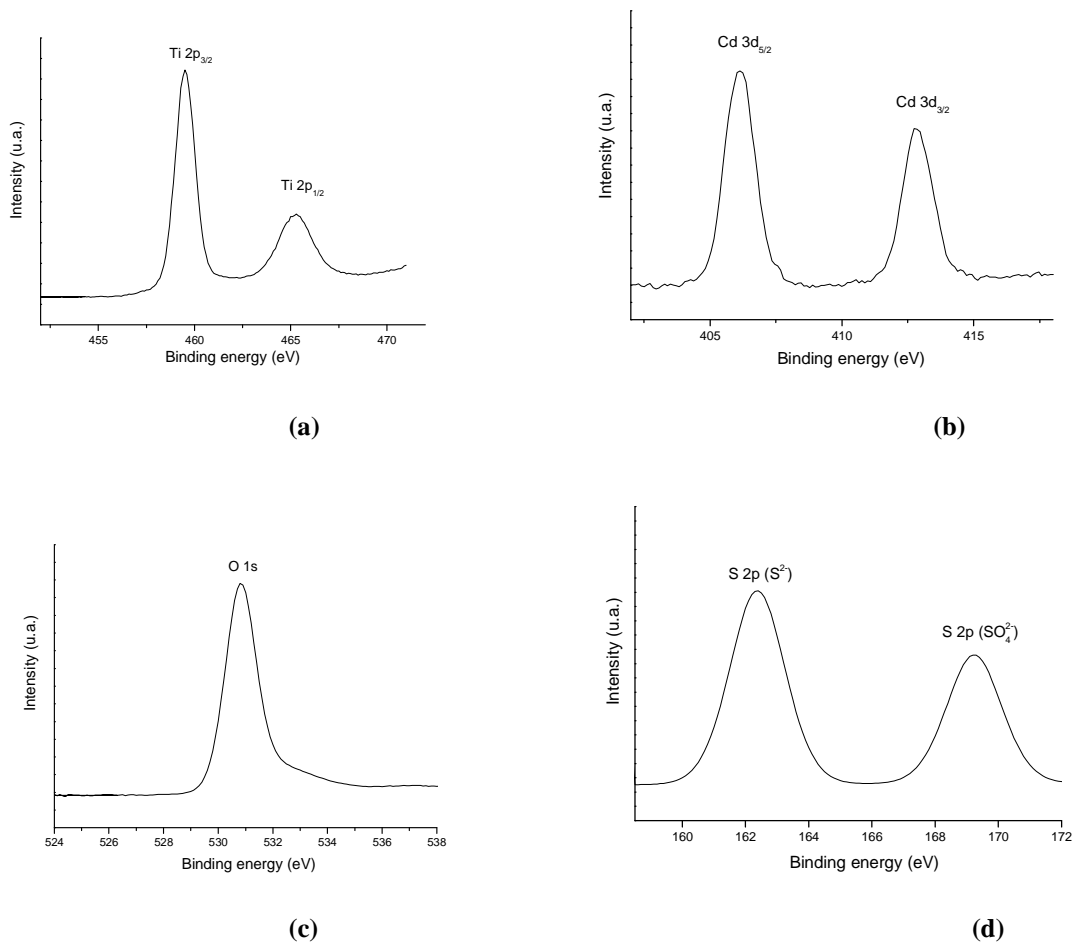
(a)

(b)

(c)

(d)

Figure 10-13 High resolution XPS spectra of Ti2p (a) Cd3d (b) O1s (c) and S2p (d).

UV-Visible spectra confrontation between Ti/TiO$_2$ sheet and Ti/TiO$_2$/CdS sheet is shown in Figure 10-14. One can notice that the sample containing CdS nanoparticles presents a shift of the absorbance peak compared with reference sample; 440 nm (Ti/TiO$_2$/CdS) and 300 nm (Ti/TiO$_2$) respectively. The shift of the absorption peak to the near visible region may be due to the presence of the CdS nanoparticles and their sensitization effect in the visible region. One can also to notice, for the TiO$_2$/CdS, a smaller peak of absorption located in the UV region, around the characteristic absorption wavelength of the TiO$_2$, this may be due to the TiO$_2$ under the QDs layer. This presence leads to an absorption also in the UV spectra. A better light absorption in the near visible region is hoped result, in order to increase the light harvesting in the near visible and consequently enhance the efficiency of the water splitting device.
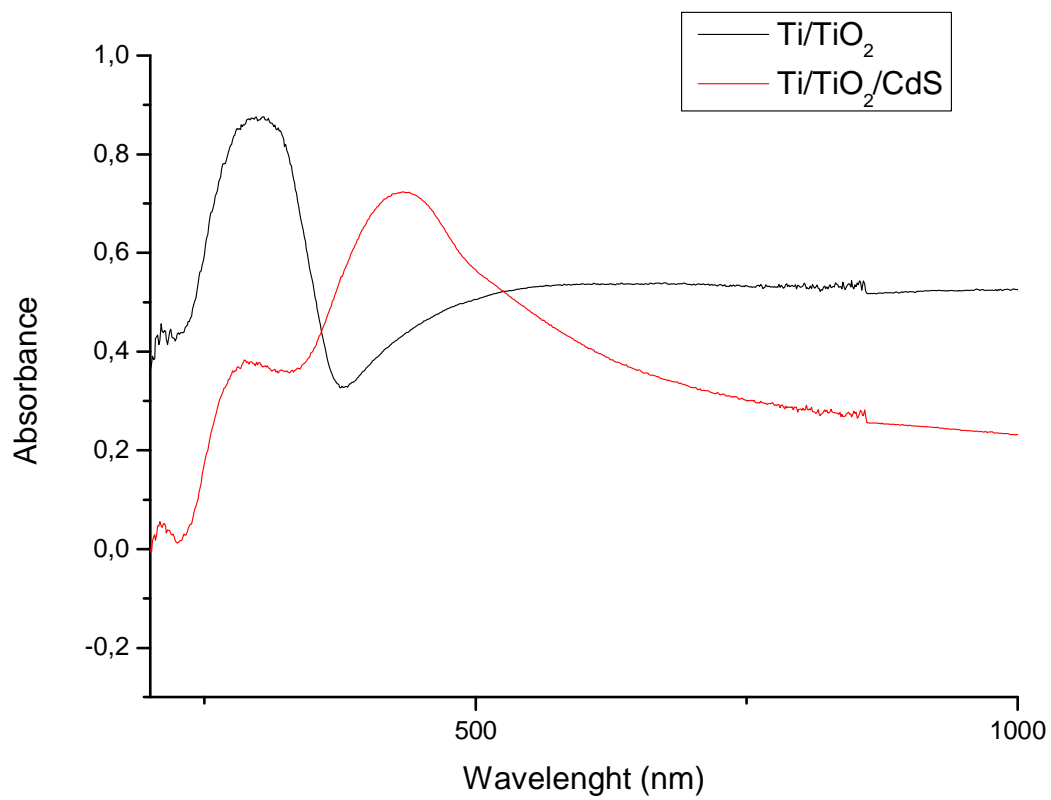
Figure 10-14 UV- Visible absorption spectra confrontation between Ti/TiO$_2$ sample (black) and Ti/TiO$_2$/CdS (red).

11. Photoelectrochemical tests (PEC)

In this chapter the photoelectrochemical PEC test carried out on the produced samples are presented. The experiment device, configuration and parameters are described for both tests done: cyclic voltammetry and chronoamperometry. Then, my results obtained are presented and commentated considering the aims of this work.

11.1. Photoelectrochemical techniques

Photoelectrochemical techniques were carried out in a three-electrode configuration with our prepared sample as working electrode, Pt rod as counter electrode and saturated calomel electrode as reference electrode, Figure 11-2. An aqueous solution of Na_2SO_4 0,5 M (pH=7) was used as electrolyte and sacrificial agent in order to maintain the stability of CdS. Before the experiment, the solution was purged with argon in order to remove the dissolved oxygen. A 150 Watt Xenon short-arc XBO lamp equipped with a AM 1.5 G filter was used as illumination source for simulate the solar light. For these tests we employed a quartz cell specifically designed (Figure 11-1 (b)) with a window of 70 mm^2 area. The window was necessary for illuminate a controlled and constant portion of the sample. The lamp was positioned at a fixed distance (30 cm) from the cell Figure 11-1 (b) and the lamp's power fixed at 150 W. The experiment configuration and disposition is shown in Figure 11-3. Two different tests were carried out: cyclic voltammetry and chronoamperometry in order to check and monitor the photosensitization of the TiO_2 NFs by CdS NPs.
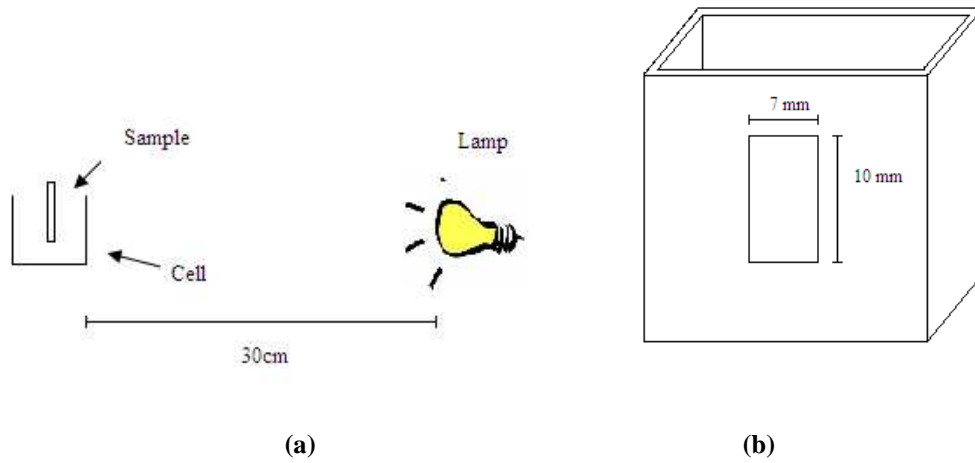
(a)   (b)

Figure 11-1 Schematic representation of the lamp distance (a) and the cell employed (b) for the photoelectrochemical tests.

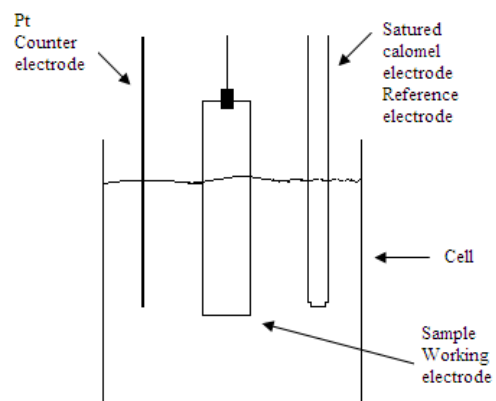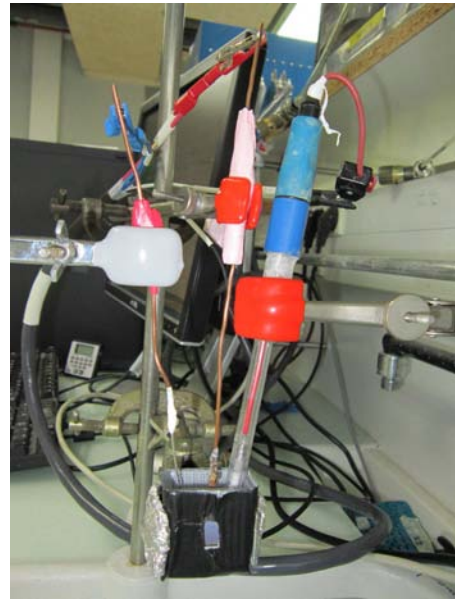**Figure 11-2 Schematic representation of disposition of the three-electrodes configuration in the cell.**

(a)   (b)

Figure 11-3 (a) Equipment used for the PEC tests (behind the paper box there is the lamp) and (b) detail of the cell with the electrodes.

11.1.1.   Cyclic voltammetry

In cyclic voltammetry, the working electrode potential increased linearly with the time until a fixed potential. When the set potential is reached the working electrode's potential ramp is inverted, that could happen several times in the same experiment; in our case the inversion is done only once. The potential range of the measure is from -0,6 V to 0,6 V and the potential increasing rate is equal to 10,00 mV/s. The experimental current is plotted as a function of the applied voltage giving a voltammogram curve. Then, the current data were divided by the value of the window area, in order to obtain the current density i in $\mu A/cm^2$. In order to check the sensitization efficiency, voltammograms were recorded both for TiO_2 NFs alone and for NFs impregnated with CdS QDs (41). Moreover, to test the suitability of these samples for photoelectrochemical cell these measurements were done both in dark and under simulated solar light illumination conditions. We are expecting an increase of the photocurrent under illumination and for the samples impregnated with CdS QDs. A higher photocurrent would correspond to a higher efficiency of the device for solar hydrogen generation.

The ideal behaviour of a n-type semiconductor electrode in dark condition and under illumination is shown in Figure 11-4. At the flat band potential there is no current, either in dark or upon irradiation (Region II), because there is no electric field to separate the generated charge carriers. At potentials negative respect the flat band potential (Region I) an accumulation layer exist and the electrode can act as a cathode both in dark and upon illumination conditions. At potentials more positive than the flat band potential (Region III) a depletion layer is formed, hence there is no oxidative current in dark. However upon irradiation a photo-current can be observed since a part of the energy required for the oxidation is provided by the radiation, via the production of the holes (42).
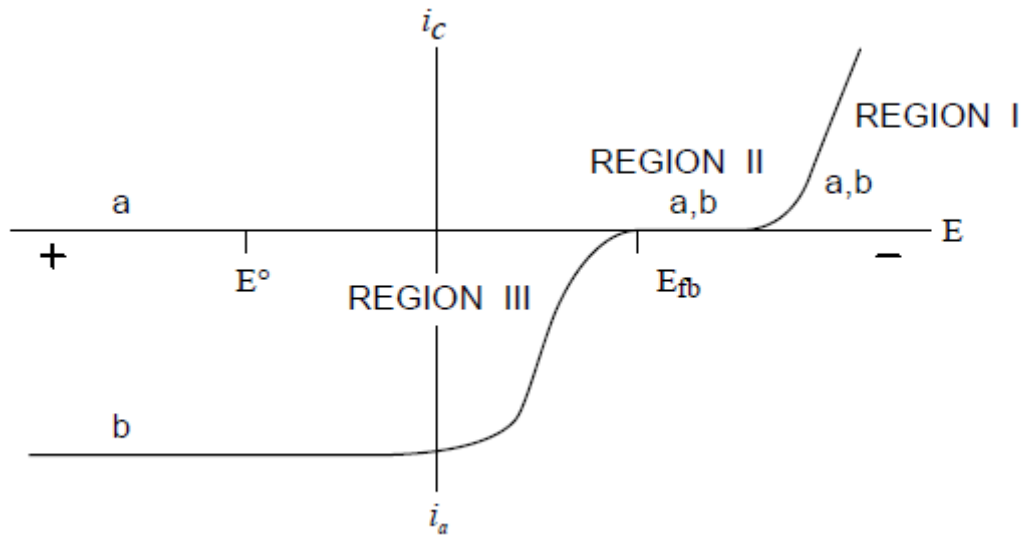
Figure 11-4 Ideal behaviour of a n-type semiconductor in dark (a) and under illumination (b) (42).

11.1.2. Chronoamperometry

Chronoamperometry is an electrochemical technique in which the potential between the working electrode and the reference electrode is maintained constant and the current is measured as a function of time. The experimental values of the current were divided by the value of the window area (0.7 cm^2) in order to obtain the current density i in μA/cm^2. During this test we measured the variation of the current as a function of the time, modifying the illumination of the sample. Or rather, the illumination of the sample was turned off and turned on for 20 seconds every 20 seconds and the variation of photocurrent was measured meanwhile the sample was subjected to a cyclic illumination, the entire measure goes on for five minutes. In this way it was possible to verify the stability of the electrodes during several cycles of illumination. Furthermore, we compared the results obtained with TiO$_2$ NFs sheet with and without CdS QDs to evidence the sensitization phenomenon. The measures were recorded fixing the potential at 0 V and 0,5 V.

Figure 11-5 presents an idealized photocurrent profile. Immediately when the electrode is illuminated the photo-induced separation of the electron-hole pairs led to a relatively large photocurrent peak. Then, the peak decays, the decrease of the photocurrent indicates that recombination of the electron-hole pairs occurs. Charge carriers which are generated deep inside the film take a longer time to reach the surface than those generated close to the surface, consequently they are more probably lost for recombination. The degree of the recombination with respect to the generation of the electron-hole pairs determines the rate of the photocurrent decay. A stable current is achieved once the charge generation and recombination reach the equilibrium (43). In our case we fixed the cycles of illumination at 20 seconds, this period of time should permit to reach a stable current and hence to reach the equilibrium between the two opposite processes. Studying the current decay profile is possible to get an idea of the electron-hole pairs production and recombination mechanisms.
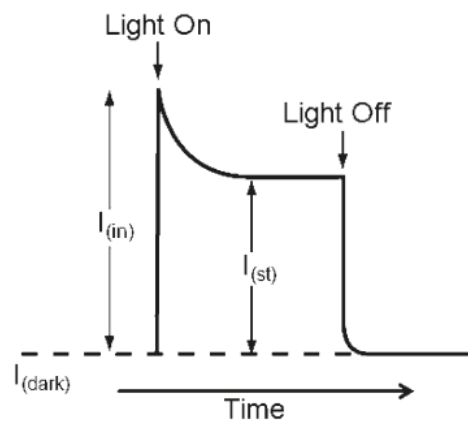
Figure 11-5 Schematic profile of the photocurrent decay under illumination (43).

11.2.   Results

In this section are presented the results recorded during the PEC tests. We used the TiO_2 NFs sheet as a reference to evidence the photosensitization effect with the addition of CdS QDs. The outcomes are organized in two chapters concerning the techniques used.

11.2.1.   Cyclic voltammetry

Figure 11-6 presents the results obtained with Ti/TiO_2 sheet under illumination and in dark conditions, used as a reference. One can see that the variation of the photocurrent density measured as a function of the potential vs calomel electrode for the curve under light illumination (red curve), reaching the value of 151 $\mu A/cm^2$ at 0.6 V vs calomel electrode. In the other hand the same test carried out for the same sample under dark conditions (black curve) does not show any relevant increase of the current density for positive voltage values which remains close to $i = 0$ $\mu A/cm^2$.

In Figure 11-7 are shown the results obtained during the analysis of $Ti/TiO_2/CdS$ sample in both conditions: under illumination and in dark. Once again, it is possible to notice the different behaviour of the sample. Under illumination, increasing the potential vs calomel electrode the measured current density is raising until reaching 1641 $\mu A/cm^2$ at 0.6 V vs calomel electrode. In the other hand the measure recorded for the same sample under dark conditions results in a flat curve standing around $i = 0$ $\mu A/cm^2$. These measures evidence the influence of the light illumination on the photoelectrical behaviour of the produced samples and its light sensitive properties.
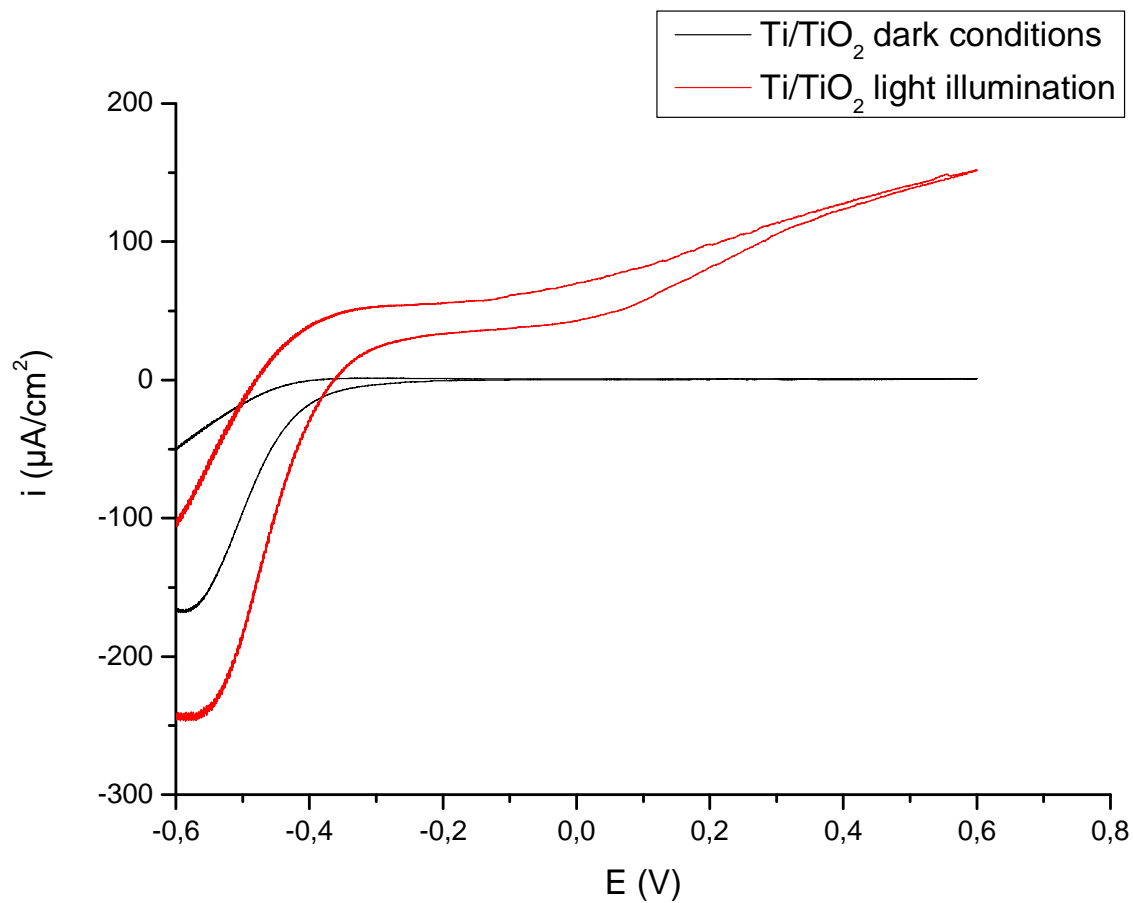
Figure 11-6 Voltammogram of the Ti/TiO$_2$ sheets in dark condition and under illumination.
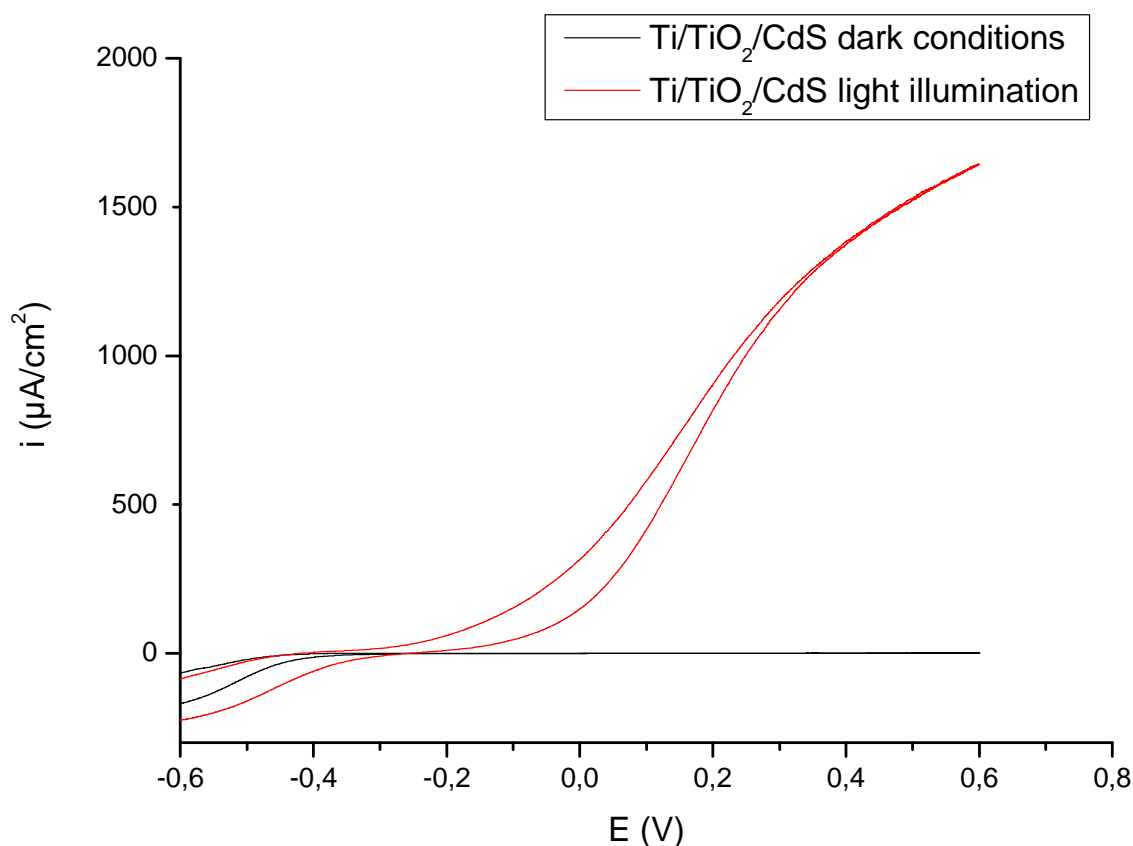
Figure 11-7 Voltammogram of the Ti/TiO$_2$/CdS in dark condition and under light illumination.

In order to check that the introduction of the CdS QDs on the TiO$_2$ NFs porous nanostructure is really increasing the light harvesting and improving the photo-response of the sample, a confrontation between the curves obtained for Ti/TiO$_2$ sheet and Ti/TiO$_2$/CdS sheet under illumination condition has been made. The results are presented in Figure 11-8. One can easily notice the higher current density reached by the sample containing the CdS QDs, 1641 µA/cm^2 at 0.6 V vs calomel electrode against 151 µA/cm^2 for the sample without CdS (for the same value of the applied potential).

The increase of the experimental current was an expected result, evidencing that CdS QDs are effectively sensitizing the TiO$_2$ NFs, allowing a better light harvesting and the achievement of a higher produced photocurrent. An higher value of the photocurrent would correspond to an higher number of electrons produced and employed to reduce the H$^+$ into H$_2$ at the cathode, improving the efficiency of the hydrogen producer device.
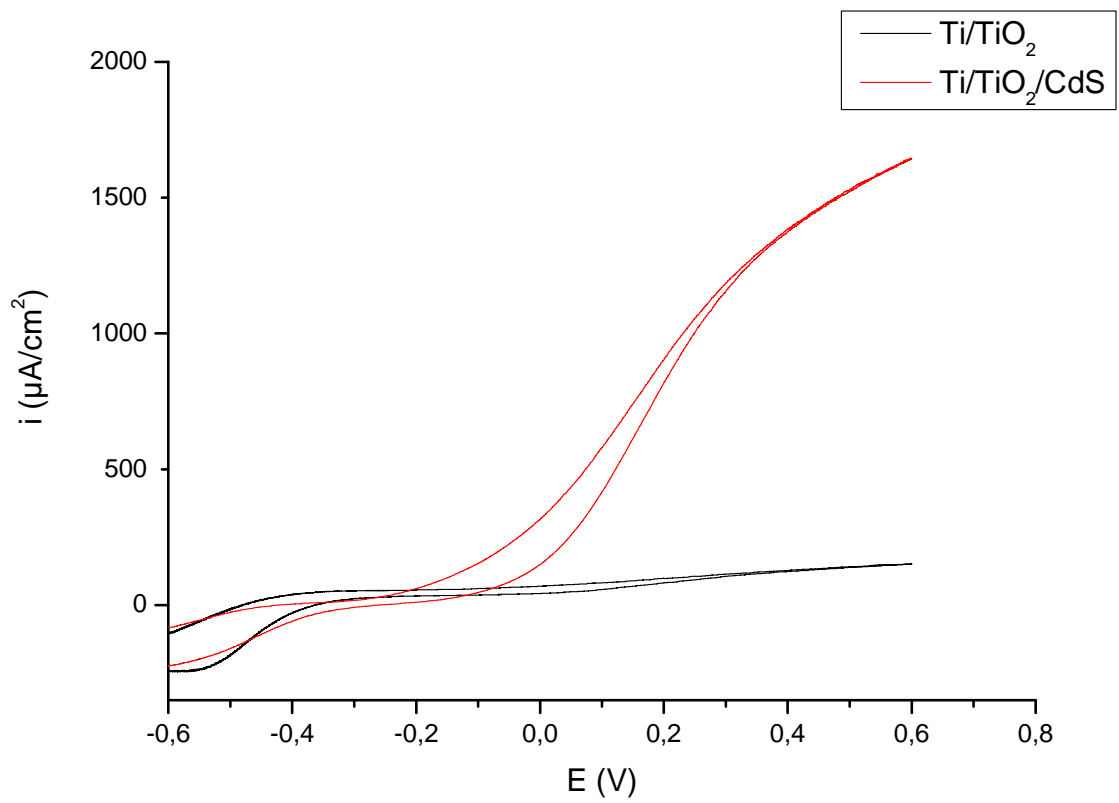
Figure 11-8 Confrontation of the curves of Ti/TiO$_2$ sheet and Ti/TiO$_2$/CdS sheet under illumination.

11.2.2.   Chronoamperometry

Figure 11-9 shows the plot obtained measuring the current density as a function of time at a fixed potential of 0 V vs calomel electrode. The graph was obtained stopping the light illumination for 20 seconds every 20 seconds and the test is conducted for 5 minutes. Firstly, one can see how the experimental current measured between the working electrode and the counter electrode is nearly zero in dark condition and is significantly increased after illumination for both the tested samples (with and without QDs), this reveals a good photo-response and highlights the ability of the device to produce current under illumination. Moreover, we notice a relevant increase of the current density for the sample containing CdS QDs over the surface, which reaches 200 $\mu A/cm^2$, compared with 53 $\mu A/cm^2$ reached by Ti/TiO$_2$ sample. These values were obtained from the graph after the stabilization of the two competitive processes of the electron-hole pairs creation and recombination. This data evidence one more time the successful sensitization effect of the TiO$_2$ NFs by the CdS QDs and confirm their improvement in the light harvesting ability of the sample.

The analysis of the current density profile under illumination gives information on the different behaviours of the two samples. In the case of Ti/TiO$_2$/CdS sheet the decay profile of the current density presents an initial peak due to the quick electron-hole production, followed by a sudden decrease, associated to their fast recombination. This behaviour of the current density decay fits pretty well with the ideal profile showed in Figure 11-5. In the other hand the Ti/TiO$_2$ sheet the current density evolution follows a different trend. In this case is present an initial peak followed by a sudden decay and a progressing enhancement of the current. This was not expected and may be due to the different rates of the electron-hole pairs production and recombination processes considering the sample containing QDs.

Another remarkable result is the reproducibility of the measures, for both the samples tested after eight cycles of illumination the profile and the final current density value remain pretty much the same. Only a small decrease of the current density value after five minutes has been recorded. This evidences unambiguously the reproducibility and the stability of the sample's behaviour during several illumination cycles and checks the non degradation of the electrode.
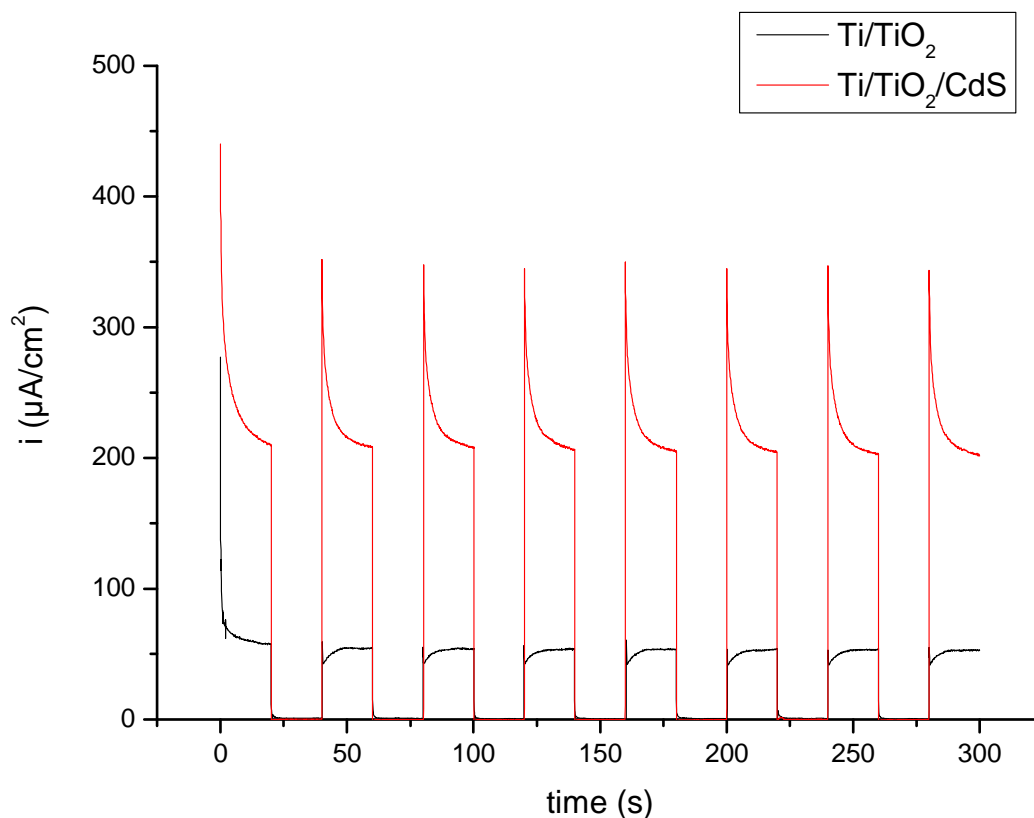
Figure 11-9 Chronoamperometry plot produced fixing the potential at 0 V vs calomel electrode.

In Figure 11-10 are showed the results obtained for the same test carried out at 0.5 V vs calomel electrode. Here are confirmed some results obtained with the measure at 0 V vs calomel electrode; e.g. the good photo-response of the samples under illumination conditions, especially for the one containing CdS QDs. The improvement of the light harvesting ability adding CdS QDs and resulting in a bigger current density under illumination is also proved.

The values obtained after stabilization of the current density are: 140 $\mu A/cm^2$ for the Ti/TiO$_2$ sample and for 1535 $\mu A/cm^2$ the Ti/TiO$_2$/CdS sample. The reproducibility and the stability of the process is also confirmed in the time range of the test.

The main difference noticed here concerns the current density evolution under illumination. For the Ti/TiO$_2$ sample the decay of the current density is not significant and its value is approximately constant until the end of the illumination. In the other

83

hand, the sample containing CdS QDs shows an initial small peak followed by a weak decay of the current density reaching suddenly a stable value. This reflect the ideal profile showed in Figure 11-5 although it is slightly different compared to the profile measured at 0 V vs calomel electrode, especially in the decay velocity of the current density. As one can see, the current density decay for the test carried out at 0.5 V is lower compared to the drop after the initial peak registered for the test at 0 V and even negligible for Ti/TiO_2 sample at 0.5 V. The results suggest that the evolution of the process of production-recombination of the electron-hole pairs is different, in particular the recombination process appear to be slower in these conditions. This may be due to the higher voltage applied which drags rapidly the electrons through the TiO_2/CdS structure avoiding the recombination of the electron-hole couples and leading to a lower decay of the current.
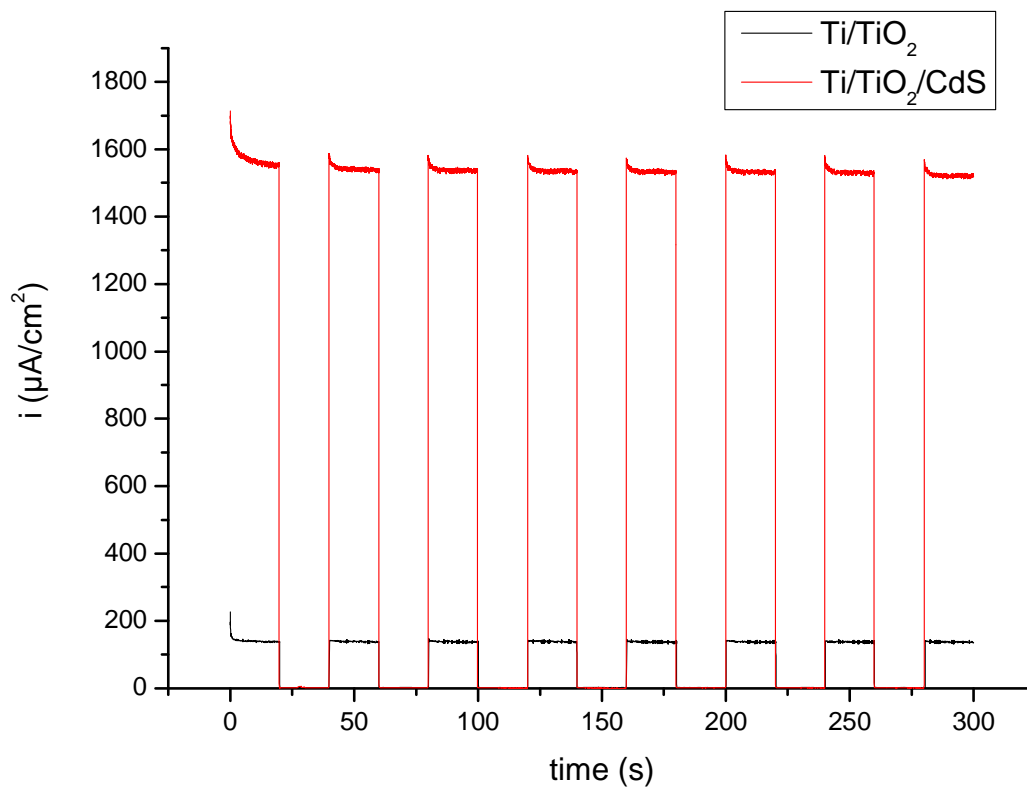

Figure 11-10 Chronoamperometry plot obtained fixing the potential at 0,5 V vs calomel electrode.

Figure 11-11 shows a long duration test for the sample Ti/TiO$_2$/CdS performed at the fixed potential of 0 V. It follows the same procedure than the previous tests, except the longer time of the measure. We performed it for 30 minutes in order to check the stability of the reactions that leads to the production of the electron-hole pairs. As it is possible to see, after an initial decay the measured current density reach a stable value; approximately after 900 seconds. This result shows that our photo-anode can resist well to the photo-corrosion and that the current produced remains stable after 45 cycles of switching on and off of the lamp.

The initial decay of the current may be explained considering that the electrolyte has not been purged with Ar during the test but only before it, this fact can be explained considering the small dimensions of the cell employed. At the photo-anode, we have a production of O$_2$ and without the gurgle of Ar the concentration of O$_2$ in the electrolyte increases. This accumulation of O$_2$ dissolved in the electrolyte may prevent the production of O$_2$ at the photo-anode and therefore condition all the processes inside the photo-electrochemical cell. We can conclude that our photo-anode presents good stability, reproducibility and good resistance to the reactions taking place over its surface.
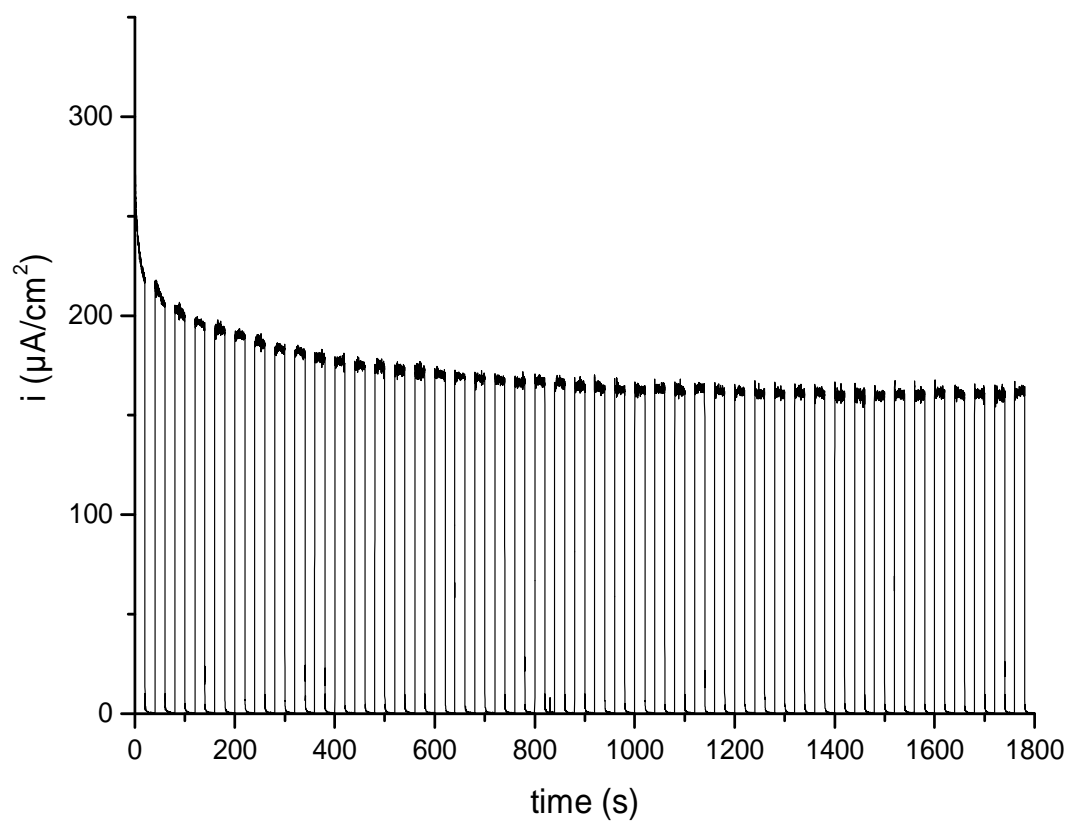
Figure 11-11 Chronoamperometry plot for the Ti/TiO$_2$/CdS sample test (long duration).

12. Conclusions

The presented thesis focuses on the realisation of efficient photo-anodes employed for photo-electrochemical hydrogen production by water splitting. We produced TiO_2/CdS nanocomposites over a Ti substrate coupling TiO_2 nanofibers with CdS quantum dots in order to use them as photo-anode. We tried to produce separately the nanofibers and the quantum dots and later to couple them. TiO_2 was chosen for its photo-activity, its chemical stability and its photo-corrosion resistance. The CdS quantum dots where added in order to shift the absorbance of the TiO_2 to the near visible region, increasing in this way the light harvesting of the device and therefore the efficiency of the cell employed for hydrogen production. It is possible to divide the work in two main parts: the first one may be identified in the production of the photo anodes while the second one may be identified in the realization of the characterization and the photo-electrochemical tests; followed by the analysis of the results obtained.

The production section is focused on the preparation of the nanocomposite photo-anode. The CdS quantum dots were produced by polyol process (discussed in chapter 8.1), in this case, we obtained CdS quantum dots with an average diameter of 3.6 nm. Separately, the TiO_2 nanofibers where grown over a Ti sheet by hydrothermal method (discussed in chapter 8.2), we have been able to obtain a complex structure made up of branched TiO_2 nanofibers. The last production step of the photo-anode is the coupling of the nanofibers with the quantum dots by impregnation method. In this last step the Ti/TiO_2 sheet was dived into a polyol based solution of quantum dots for a fixed time.

The second section is focused on the characterization and photo-electrochemical tests results. The characterization can be divided in three different parts related to the three steps of the production: the CdS quantum dots characterization, the TiO_2 nanofibers characterization and finally the TiO_2/CdS nanocomposite characterization. For characterize CdS QDs we performed TEM image observations in order to determine the average diameter, XRD analysis to identify the crystalline phases and finally UV-Visible analysis for the calculation of the gap. SEM and TEM pictures of the TiO_2 NFs were recorded in order to study their morphology, XRD analysis in order to determined the crystalline phase and UV-Visible analysis for the band gap calculation. Finally SEM and TEM observations of the TiO_2/CdS nanocomposite were performed in order to describe

the morphology of the materials, UV-Visible analysis to check the shift in the absorbance and XPS analysis in order to ensure us about the effective deposition of the QDs over the NFs.

Thanks to all these techniques we can affirm that we have been able to produce Ti/TiO$_2$/CdS nanocomposites over a Ti substrate, with good adhesion of the QDs over the NFs. This functional material can be used as photo-anode in photo-electrochemical cells for hydrogen production.

In order to test the photo-response of the produced samples, photo-electrochemical tests were carried out. We focused over two techniques: cyclic voltammetry and chronoamperometry. Cyclic voltammetry was performed in dark and illuminated conditions for both the samples, with or without QDs. It permits us to measure the current density scanning the voltage in a fixed range. The results show the different behaviour of the samples in dark and illuminated conditions confirming the photo-activity of both the samples, with and without QDs. Moreover, the confrontation between the two samples under illumination conditions shows that the presence of CdS QDs actually enhances the measured current density. This was an expected result; an increase of the current density under illumination may be considered as a proof of the improvement of the light harvesting ability of the sample adding CdS. The second technique employed, chronoamperometry, consists in the measure of the current density as a function of the time fixing a predetermined voltage. During the test, we switched on and off the light with intervals of 20 seconds; being the total duration of the test 5 minutes. This test, beyond to confirm one more time the photo-response of the samples with an increase of the photo-current under illumination, permits to check the stability and reproducibility of the processes involved in the photocurrent production. The test has been carried out fixing two different values of the potential: 0 V and 0.5 V. In both cases, we observed a remarkable increase of the photo-current under illumination, with an higher value for the sample containing QDs. Moreover, the photo-current evolution during each illumination step is constant; this result shows that the processes involved are consistent and stable for all the duration of the test. A long term test was carried out on the sample containing CdS quantum dots; we maintained the parameters of the previous chronoamperometry tests at 0 V and we extended the duration of it until 30 minutes in order to check the resistance of the photo-anode to several cycles (in this case 45) of switch on and off the light. It is

possible to observe that after an initial decay, the photo-current reach a stable value, maintained until the end of the test.

To conclude, we have been able to develop an easy and reproducible way to produce TiO$_2$/CdS nanocomposite photo-anodes over a Ti substrate which can be employed in solar hydrogen production applications. The production techniques employed allow the possibility to scale-up the production, feature that could be interesting for a future commercial application. Moreover, we confirmed that coupling TiO$_2$ NFs with CdS QDs is possible to enhance the light harvesting of the TiO$_2$ shifting its absorbance to the near visible region of the solar spectrum.

In this way it is possible to increase the photo-current produced and used for split the water molecule and consequently increase the efficiency of the photo-electrochemical cell. Moreover, our photo-anode shows all characteristics of stability and resistance to several cycles of switch on and off the illumination.

More work can be done setting and optimizing the parameters (temperature, time, quantities of the reagents, etc.) of the different production steps in order to obtain a micro and nano structure able to maximize the produced photocurrent. Moreover, it may be interesting to quantify the effective quantity of QDs deposed over the fibres, we tried to carry out XPS analysis but several problems occurred.

13. References

(1) Fujishima A, Honda K. (1972). Electrochemical Photolysis of Water at a Semiconductor Electrode *Nature* **238**: 37

(2) Nejat Veziroglu T., Sumer Sahn (2008). 21st Century's energy: Hydrogen energy system Energy Conversion and Management **49** :1820–1831

(3) New York State Energy Research and Development Authority (2005) *Hydrogen fact sheet* (USA)

(4) Priddle R. (2002) Beyond Kyoto energy dynamics and climate stabilization. International Energy Agency OECD/IEA

(5) http://www1.eere.energy.gov/hydrogenandfuelcells/production/index.html

(6) Becquerel E. (1839). Mémoire sur les effets électriques produits sous l'influence des rayons solaires *Compt Rendues* **9**: 561-567

(7) Brattain, W.H., Garrett, C.G.B. (1955). Experiments on the Interface Between Germanium and an Electrolyte *Bell System Techn. J.* **34**: 129

(8) Gerischer H. Z. (1960) Kinetics of oxidation-reduction reactions on metals and semiconductors. I &II General remarks on the electron transition between a solid body and a reduction-oxidation electrolyte *Z. physik. Chem.* **26**: 223

(9) Memming R. (1969). Mechanism of the electrochemical reduction of persulfates and hydrogen peroxide *J. Electrochem. Soc*. **116**: 785 – 790

(10) Morrison SR. Electrochemistry at semiconductor and oxidized metal electrodes. *Plenum Press*. 1401

(11) Gaoling Zhao, Hiromitsu Kozuka, Toshinobu Yoko (1997). Effects of the incorporation of silver and gold nanoparticles on the photoanodic properties of rose bengal sensitized TiO2 film electrodes prepared by sol-gel method *Sol. En. Sol. Cells* **46**: 219-231

(12) Kiwi J, Gratzel K. (1986). Heterogeneous photocatalysis: enhanced dihydrogen production in titanium dioxide dispersions under irradiation. The effect of magnesium promoter at the semiconductor interface *J Phys. Chem.* **90**: 637

(13) O'Regan B., Gratzel M. (1991). A low-cost, high-efficiency solar cell based on dye-sensitized colloidal TiO2 films *Nature* **353**: 737

(14) Park J.H., Kim S.W., Bard AJ. (2006). Novel carbon-doped TiO_2 nanotube arrays with high aspect ratios for efficient solar water splitting. *Nano Lett.* **6**: 24

(15) Vogel R., Hoyer P., Weller H. (1994). Quantum-Sized PbS, CdS, Ag2S, Sb2S3, and Bi2S3 Particles as Sensitizers for Various Nanoporous Wide- Bandgap Semiconductors. *J. Phys. Chem.* **98**: 3183–3188.

(16) Bak T., Nowotny J., Rekas M., Sorrell C.C. (2002). Photo-electrochemical hydrogen generation from water using solar energy. Materials-related aspects *Int. J. of Hydrogen Energy* **27**: 991 – 1022

(17) Anderman M., Kennedy J.H., In: Finklea H.O., Semiconductor electrodes. Amsterdam: Elsevier, (1988): 147–202.

(18) Chandra S. Photoelectrochemical solar cells. New York: Gordon and Breach, (1985): 163–9

(19) Ashokkumar M. (1998). An overview on semiconductor particulate systems for photoproduction of hydrogen *Int. J. Hydrogen Production* **23**: 427-438

(20) Michael R. Hoffmann, Scot T. Martin, Wonyong Choi, Detlef W. Bahnemann (1995) Environmental Applications of Semiconductor Photocatalysis *Chem. Rev.* **95**: 69-96

(21) Grätzel M. (2001). Photoelectrochemical cells *Nature* **414**: 338-344

(22) Honda K. In: Ohta T, Solar-Hydrogen Energy Systems. Oxford: Pergamon Press, (1979): 137–69.

(23) Ram B. Gupta, Hydrogen Fuel: Production, Transport, and Storage

(24) Carp O., Huisman C.L., Reller A. (2004). Photoinduced reactivity of titanium dioxide *Progress in Solid State Chemistry* **32**: 33–177

(25) Jiefang Zhu , Michael Zäch (2009). Nanostructured materials for photocatalytic hydrogen production *Current Opinion in Colloid & Interface Science* **14**: 260–269

(26) Xu C, Shaban YA, Ingler WB, Khan SUM. (2007). Nanotube enhanced photoresponse of carbon modified (CM)-n-TiO_2 for efficient water splitting. *Sol Energy Mater Sol Cells* **91**:938.

(27) Bamwenda G.R., Tsubota S., Nakamura T., Haruta M. (1995). Photoassisted hydrogen production from a waterethanol solution: a comparison of activities of Au-TiO2 and Pt-TiO2. *J Photochem Photobiol A: Chem* **89**:177

(28) Choi W.Y., Termin A., Hoffmann M.R. (1994). The role of metal ion dopants in quantum-sized TiO2: correlation between photoreactivity and charge carrier recombination dynamics. *J Phys Chem* **98**:13669–13679

(29) Meng Ni, Michael K.H. Leung, Dennis Y.C. Leung, K. Sumathy (2007). A review and recent developments in photocatalytic water-splitting using TiO2 for hydrogen production Renewable and Sustainable Energy Reviews **11**: 401–425

(30) R. Asahi, T. Morikawa, T. Ohwaki, K. Aoki, Y. Taga (2001). Visible-Light Photocatalysis in Nitrogen-Doped Titanium Oxides *Science* **293**: 269-271

(31) Takeuchi M., Yamashita H., Matsuoka M., Anpo M., Hirao T., Itoh N. (2000). Photocatalytic decomposition of NO under visible light irradiation on the Cr-ion-implanted thin TiO2 thin film photocatalyst. *Catal Lett* **67**:135–7

(32) Jana AK. (2000) Solar cells based on dyes. J *Photochem Photobiol A: Chem* **132**: 1–17

(33) Fiévet F., Brayner R. Nanomaterials: A Danger or a Promise, The Polyol Process (2012)

(34) K. Byrappa a, T. Adschiri (2007). Hydrothermal technology for nanotechnology *Progress in Crystal Growth and Characterization of Materials* 53: 117-166

(35) Hsin-Hung Ou, Shang-Lien Lo (2007). Review of titania nanotubes synthesized via the hydrothermal treatment *Fabrication, modification, and application Separation and Purification Technology* **58**: 179–191

(36) Liji Sobhana S.S, Vimala Devi M., Sastry T.P., Asit Baran Mandal (2011). CdS Quantum dots for measurement of the size dependent optical properties of thiol capping *j. Nanopart Res* **13**:1747-1757

(37) Vineet Singh, Pratima Chauhan (2009). Structural and optical characterization of CdS nanoparticles prepared by chemical precipitation method *J. Physics and Chemistry of Solids* **70** 1074–1079

(38) Brus L. E., (1984). Electron–electron and electronhole interactions in small semiconductor crystallites: The size dependence of the lowest excited electronic state *J. Chem. Phys*. **80**: 4403

(39) Lopez R., Gomez R., (2012). Band-gap energy estimation from diffuse reflectance measurements on sol–gel and commercial TiO2: a comparative study J. *Sol-Gel Sci. Technol*. **61**: 1–7

(40) Zhu J., Yang D., Geng J., Chen D., Jiang Z. (2008) Synthesis and characterization of bamboo-like CdS/TiO2 nanotubes composites with enhanced visible-light photocatalytic activity *J. Nanopart. Res.* **10**:729–736

(41) Luo J., Ma L., He T., Fan C., Wang S., Sun H., Jin Fan H. (2012). TiO2/(CdS, CdSe, CdSeS) Nanorod Heterostructures and Photoelectrochemical *Properties J. Phys. Chem.* **116**: 11956–11963

(42) Adrian W. Bot (1998) Electrochemistry of Semiconductors Current Separations **17**: 3

(43) Nicholas J. Bell, Hau Y., Du A., Coster H., Smith S. M., Amal R. (2011). Understanding the Enhancement in Photoelectrochemical Properties of Photocatalytically Prepared TiO2-Reduced Graphene Oxide Composite *J. Phys. Chem.* **115**: 6004–6009